VIROLOGY

# EphrinB2 clustering by Nipah virus G is required to activate and trap F intermediates at supported lipid bilayer–cell interfaces

**Joyce J. Wong[1]*†, Zhongwen Chen[2,3†], Jean K. Chung[3‡], Jay T. Groves[3§], Theodore S. Jardetzky[1§]**



**Paramyxovirus membrane fusion requires an attachment protein that binds to a host cell receptor and a fusion protein that merges the viral and host membranes. For Nipah virus (NiV), the G attachment protein binds ephrinB2/B3 receptors and activates F-mediated fusion. To visualize dynamic events of these proteins at the membrane interface, we reconstituted NiV fusion activation by overlaying F- and G-expressing cells onto ephrinB2-functionalized supported lipid bilayers and used TIRF microscopy to follow F, G, and ephrinB2. We found that G and ephrinB2 form clusters and that oligomerization of ephrinB2 is necessary for F activation. Single-molecule tracking of F particles revealed accumulation of an immobilized intermediate upon activation. We found no evidence for stable F-G protein complexes before or after activation. These observations lead to a revised model for NiV fusion activation and provide a foundation for investigating other multicomponent viral fusion systems.**

## INTRODUCTION

Enveloped viruses have evolved a variety of proteins and mechanisms to enable virus–cell membrane fusion and entry into cells. Many enveloped viruses such as influenza virus or HIV encode a single protein that mediates this entire process, including receptor binding, lipid bilayer fusion, and virus entry (*1*, *2*). Folding of these entry glycoproteins to a metastable state primes the virus to carry out membrane fusion at the right time and right place. Activation by receptor binding for HIV env, or the low pH of endosomes for influenza virus hemagglutinin (HA), initiates large conformational changes that drive membrane bilayer fusion (Fig. 1A). The direct coupling of the triggering event (e.g., receptor binding or protonation) to the activation and refolding of membrane fusing domains within the same protein provides a tight mechanistic linkage for this type of single-component entry machinery. However, many other enveloped viruses responsible for substantial morbidity in humans, including the herpesviruses and paramyxoviruses, use multiple viral proteins to mediate entry (*3*, *4*). In these multicomponent viruses, the processes of receptor binding and membrane fusion are separated into two or more distinct viral proteins, and the triggering mechanisms and interactions that regulate fusion activation remain incompletely understood. Here, we have examined the mechanism of Nipah virus (NiV) membrane fusion activation, as a representative member of the multicomponent fusion machinery found in the broader paramyxovirus family.

The entry of paramyxoviruses into cells and the formation of cell-cell syncytia during infection require both fusion (F) and attachment glycoproteins (Fig. 1B). The F proteins are trimeric, class I viral fusion proteins that display a globular head domain attached to the membrane by a C-terminal α-helical stalk (*5*). The attachment glycoproteins are type II membrane proteins, which are tetramerized through their N-terminal α-helical stalk domains (*6*, *7*) and which bind to specific host cell receptors using their C-terminal globular head domains (*8*). In current models for paramyxovirus entry (*8*, *9*), receptor binding to the attachment glycoprotein is thought to promote conformational changes that move head domains away from the stalk domain (Fig. 1B), enabling contacts with F that trigger its refolding (*10*–*12*). The F protein mediates fusion by insertion of its hydrophobic fusion peptides (*13*) into the target host membrane, undergoing a large pre- to postfusion conformational change analogous to other class I viral fusion proteins (*3*). This results in the assembly of two heptad repeats (HRA and HRB) within the F protein into a six-helix bundle and the merging of the viral envelope and target cell membranes (Fig. 1B).

Many experiments point to the requirement for a direct and specific interaction between paramyxovirus F and attachment glycoproteins to activate membrane fusion. Fusion activation occurs only when pairs of F and attachment proteins are derived from the same or closely related viruses (*14*, *15*). Putative interaction sites on both proteins have been identified on the basis of mutagenesis and functional studies (*10*, *16*–*21*). Further evidence for F-attachment protein interactions comes from coimmunoprecipitation (*22*–*24*), colocalization of fluorescence protein-tagged fusion and attachment proteins in neurons, bimolecular fluorescence complementation, and antibody-mediated cocapping studies (*25*–*27*). However, biochemical reconstitution of these complexes has remained elusive.

A further mechanistic division has been made between some paramyxovirus family members based on whether their F and attachment glycoproteins are thought to interact before or after receptor binding. Measles, Nipah, and Hendra viruses have been proposed to have F and attachment glycoproteins that preassemble into complexes, which dissociate at the time of receptor binding and F activation (*23*, *24*, *28*). Other paramyxoviruses, such as Newcastle disease virus, parainfluenza virus 5, and the human parainfluenzaviruses, have been proposed to encode F and attachment proteins that lack interactions before receptor binding. Following receptor binding, the F and attachment glycoproteins of these paramyxoviruses are

[1]Department of Structural Biology, Stanford University, Stanford, CA, USA. [2]Multiscale Research Institute of Complex Systems, Fudan University, Shanghai, China. [3]Department of Chemistry, University of California, Berkeley, Berkeley, CA, USA.
*Present address: IgGenix, Inc., 329 Oyster Point Blvd., 3rd Floor, South San Francisco, CA, USA.
†These authors contributed equally to this work.
‡Present address: Department of Chemistry, Colorado State University, Fort Collins, CO, USA.
§Corresponding author. Email: jtgroves@lbl.gov (J.T.G.); tjardetz@stanford.edu (T.S.J.)

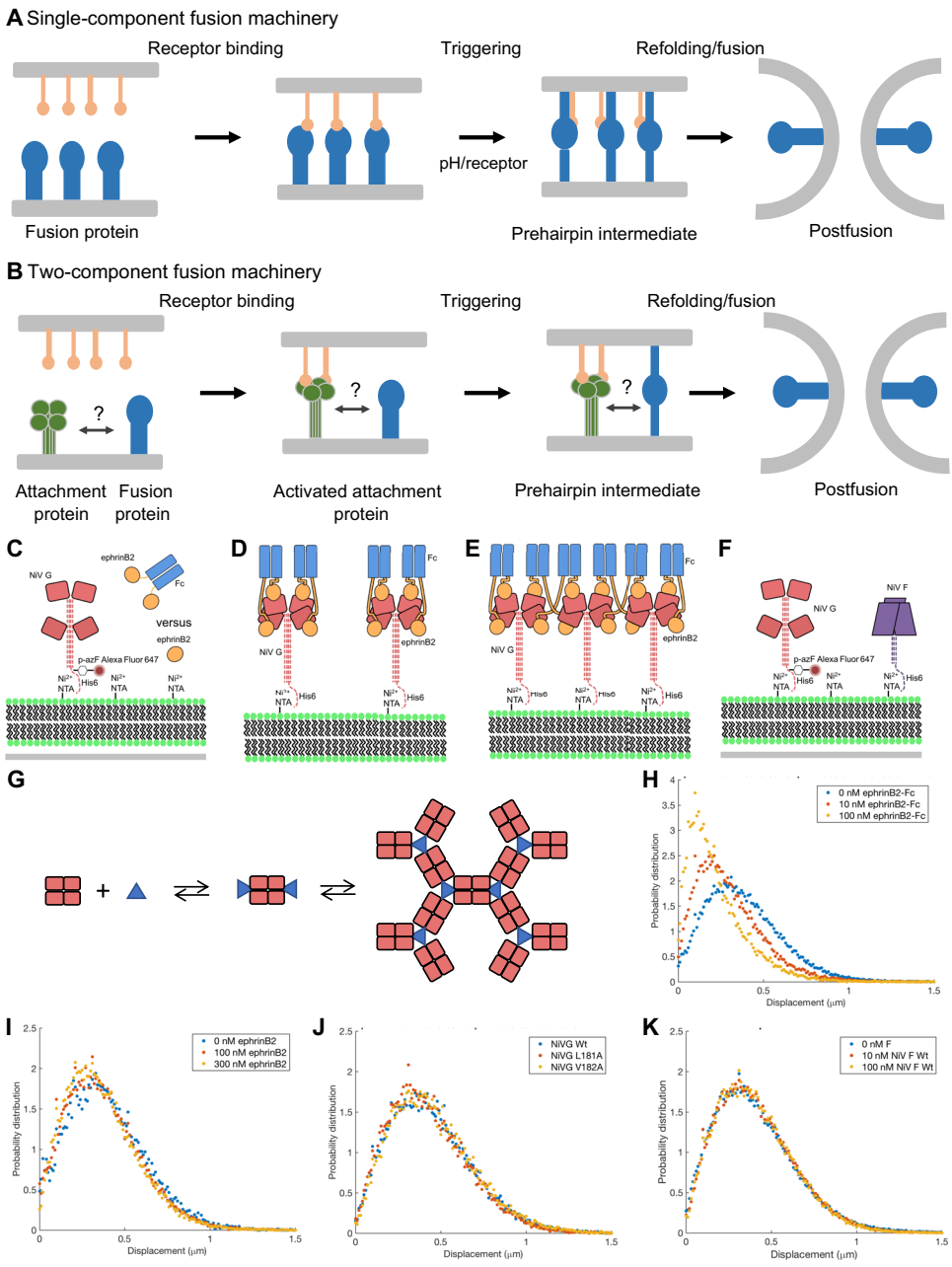


**Fig. 1. Interactions of the NiV G ectodomain on SLBs.** (**A**) Membrane fusion schematic for a single viral glycoprotein, as in HIV and influenza virus. (**B**) Schematic for two-component membrane fusion machinery, such as NiV. (**C**) Schematic of ephrinB2 binding to DIBO–Alexa Fluor 647 (AF647)–labeled NiV $G_{ecto}$ bound to Ni–nitrilotriacetic acid (NTA) on supported lipid bilayers (SLBs). (**D**) EphrinB2 monomer binding to isolated receptor tetramers. (**E**) EphrinB2-Fc dimers could lead to larger cross-linked oligomers. (**F**) Experimental setup for NiV F–NiV G ectodomain complex formation. NiV $G_{ecto}$ Wt 40 Å–p-azido-phenylalanine (pAzF) was coincubated with increasing concentrations of NiV Fecto. (**G**) Schematic of potential assemblies that could form with NiV F trimers (blue triangle) and G tetramers (tetrameric rectangle), looking down on the SLB plane. Discrete assemblies of 2:1 F:G complexes could form or progress to larger arrays of F:G complexes. (**H**) Step size distribution of NiV $G_{ecto}$ Wt 40 Å-pAzF displacements following titration with ephrinB2-Fc-mNG. (**I**) Step size distribution of NiV $G_{ecto}$ Wt 40 Å-pAzF displacements following titration of monomeric ephrinB2-167-mNG. (**J**) Step size distribution of NiV $G_{ecto}$ Wt 40 Å-pAzF, NiV G L181$A_{ecto}$ 40 Å-pAzF, and NiV G V182$A_{ecto}$ 40 Å-pAzF displacements. (**K**) Step size distribution of NiV $G_{ecto}$ Wt 40 Å-pAzF displacements following titration of NiV $F_{ecto}$.

thought to transiently interact, leading to the triggering of F conformational changes (*8*, *22*). Furthermore, it has been suggested that prolonged interactions between HPIV3 F and its attachment protein after formation of its prehairpin intermediate could play a role in "chaperoning" F through its conformational changes (*29*). Higher-order oligomerization of paramyxovirus glycoproteins either before or after receptor binding (*26*, *30*) have also been speculated to play roles in the fusion mechanism. However, prior studies have lacked sufficient spatial and temporal resolution to directly interrogate the dynamics of F-attachment glycoprotein behavior and interactions

during the process of receptor-mediated fusion activation. Thus, large gaps in our understanding of the entry mechanisms remain, which could be important to understanding virus neutralization and inhibition.

To address some of these outstanding mechanistic questions and enable direct visualization of the viral glycoprotein dynamics after receptor binding, we have reconstituted the process of membrane fusion activation for NiV using a supported lipid bilayer total internal reflection fluorescence (TIRF) microscopy approach. NiV is a member of the *Paramyxoviridae* family, closely related to Hendra and Cedar viruses. NiV is highly pathogenic, emerged recently (1998) in Malaysia, and continues to cause outbreaks, most often in India and Bangladesh (*31*, *32*). Mortality rates from the Malaysian and Bangladesh strains of NiV average at 45 and 75%, respectively (*32*). Currently, there is no vaccine or specific treatment approved for use in humans (*33*). NiV encodes a fusion (F) protein that is highly homologous to the Hendra virus F protein in sequence and structure (*34*). The NiV G protein binds to ephrinB2 or B3 receptors with high affinity (nM) and subsequent to binding activates F refolding (*35*, *36*). F and G are thought to assemble into complexes before host cell receptor binding, although recent high-resolution microscopy studies indicate that they are stochastically distributed in the cellular membrane when incorporated into budding virions (*37*).

Our TIRF microscopy approach allows the investigation of the interactions and single-molecule dynamics of NiV F and G glycoproteins, as well as the substrate-controlled manipulation of the activating receptor surface. By applying methods that have been previously developed for studies of mammalian cell-cell signaling (*38*, *39*) to the study of NiV fusion activation, we can spatially and temporally resolve the diffusion of single viral proteins during the process of activation and control the mobility of activating ephrinB2 ligands. In these experiments, NiV F– and NiV G–expressing cells are overlaid onto SLBs that present ephrinB2 receptor or other surrogate ligands. This setup recapitulates the receptor-dependent activation of F refolding and insertion into the supported bilayer in a manner that is analogous to cell:cell fusion and syncytia formation, which is associated with characteristic histopathological findings in clinical samples of NiV-infected tissues (*40*). Although we anticipated that F and G would form complexes before and potentially during fusion activation, we did not find any evidence of F association with G, either with isolated ectodomains or with full-length proteins in cells, indicating that these interactions are more dynamic than previously appreciated. Under activating conditions, we observe F insertion into the SLB and the immobilization of a substantial population of F trimers. This immobilization is not due to fusion peptide insertion into the supported bilayer, as trapping of the F prehairpin intermediate with inhibitory peptides leads to the partial recovery of F mobility. We conclude that F immobilization occurs through interactions that are dependent on the unhindered exposure of its N-terminal heptad repeat domain. Last, we studied the role of receptor oligomerization on fusion and found that clustering of ephrinB2 can be driven by G binding and that receptor oligomerization and actin polymerization are essential for F triggering.

## RESULTS

### Single-particle tracking of the NiV G ectodomain reveals interactions with bivalent ephrinB2-Fc but not NiV F

We initially set up an SLB experiment to biochemically reconstitute interactions of NiV G with ephrinB2 receptors and F (Fig. 1C) using recombinantly expressed ectodomains. Prior studies have shown that ephrinB2-Fc dimers, but not ephrinB2 monomers, induce changes in the conformation of NiV G that are thought to be further along its activation pathway, as measured by anti-G monoclonal antibody binding (*41*). EphrinB2-Fc dimers could preferentially bivalently engage single NiV G tetramers (Fig. 1D) but also have the potential to bind and cross-link multiple NiV G tetramers (Fig. 1E). In addition, we hypothesized that interactions of the F and G ectodomains that are too weak to measure in solution biochemistry experiments might be enhanced by their oriented capture to a two-dimensional planar membrane (Fig. 1F). Interactions of F trimers with G tetramers could potentially result in a heterogeneous distribution of complex stoichiometries at the bilayer surface, ranging from 1 F trimer to 1 G tetramer up to larger F-G arrays (Fig. 1G). The diffusive mobility of molecules in fluids inherently depends on their size. Although the two-dimensional nature of membranes complicates the relevant scaling relations (*42*, *43*), the general trend of reduced diffusion with larger size can still be used as a precise probe of complex formation and oligomerization in membranes (*38*, *44*, *45*). We therefore anticipated that the presence of either ephrinB2-Fc or NiV F, but not ephrinB2 monomers, would reduce the diffusion rates of NiV G by forming larger complexes on the SLBs.

For these experiments, NiV G was site-specifically labeled with Alexa Fluor 647 (AF647) through nonnatural amino acid incorporation into the linker between the stalk and N-terminal His-tag (Fig. 1C). NiV G was captured onto Ni–nitrilotriacetic acid (NTA) lipids incorporated into the SLBs at densities that allowed single-particle resolution and tracking. Trajectories of single NiV G particles were identified in videos (movie S1). Single-particle displacements during a time interval of 80 ms were measured for each particle, providing a distribution of diffusion step sizes in the presence or absence of G ligands. A shift to smaller step sizes in the NiV G displacement distribution, corresponding to reduced mobility, provides a readout of NiV G multimerization or interactions.

We observed that titration of dimeric ephrinB2-Fc causes the displacement distribution of NiV G to shift significantly to smaller step sizes (Fig. 1H and movie S2). In contrast, the titration of monomeric ephrinB2 does not affect G diffusion (Fig. 1I). The range of ephrinB2 titration concentrations was adjusted to include concentrations greater than the measured dissociation constant for each ephrinB2 construct. The shift to smaller step sizes and slower diffusion of G in the presence of ephrinB2-Fc is indicative of NiV G oligomerization, resulting in an increase in the number of lipid attachment points of the G His6-tags.

The multimerization of NiV G not only could be driven by cross-linking of the tetramers by the ephrinB2-Fc dimers (Fig. 1E) but also could potentially result from conformational changes within G that enhance tetramer-tetramer interactions. To explore these possibilities, we studied the diffusion of NiV G L181A, a mutant that reportedly adopts an activated conformation, and NiV G V182A, a mutant with enhanced fusion activity compared to wild type (*10*). We hypothesized that if intrinsic tetramer-tetramer interactions occur in activated G, then these mutants could show an enhanced tendency to oligomerize. Neither mutant showed a shift in displacement distribution relative to wt G (Fig. 1J). Overall, we conclude that the multimerization of NiV G when bound to dimeric ephrinB2 is most likely due to cross-linking and not an inherent ability of conformationally triggered NiV G to multimerize. In solution, the addition of ephrinB2 monomer at a concentration likely to saturate

all four binding sites on the tetramer is insufficient to cause multimerization of G (fig. S1A), consistent with the supported bilayer observations. In contrast, for NiV G–ephrinB2-Fc complexes formed in solution, we observe a molecular weight and saturation stoichiometry consistent with a 2:1 ephrinB2-Fc:NiV G complex (fig. S1, B to D). These data suggest that the two-dimensional confinement of NiV G leads to a cross-linking mode of ephrinB2 interaction that does not occur as readily when NiV G and ephrinB2 diffuse freely in solution.

Confinement to a two-dimensional surface imposes orientational constraints and increases the effective concentration of proteins (*45*), which could contribute to stabilizing weak interactions of NiV F and G. We measured the G step size distribution in the presence of C-terminally His8-tagged F, allowing both proteins to be bound to Ni-NTA headgroup-containing lipids in an orientation that mimics their native orientation on membranes. The increase in lipid attachment points of both proteins would contribute to decreasing observed G diffusion rates in any F-G complexes. However, no change in G diffusion was observed, indicating that no interactions between F and G ectodomains could be detected (Fig. 1K and movie S3). We confirmed that the F ectodomain is captured on the membrane, as incubation of 10 nM F on the substrate resulted in binding to the bilayer as detected by fluorescence correlation spectroscopy (fig. S2). This supports the conclusion that any potential F-G ectodomain interactions are too weak to mediate complex formation.

### Full-length NiV F and G do not colocalize in cells overlaid onto functionalized patterned SLBs

As the NiV F and G transmembrane domains and other membrane components could be necessary for their interaction, we used a TIRF microscopy setup to investigate the localization of the full-length proteins in live cells. The setup is a form of a hybrid live cell–supported bilayer junction (*46*). Relative to the preceding setup with viral protein ectodomains, it has been inverted so that the full-length viral proteins can be expressed in the cell membrane, and the supported bilayer then mimics the target cell. These experiments follow the localization of full-length G and F after cells are overlaid onto an SLB, which can be functionalized with ligands for either F or G (Fig. 2A). Cells are transfected with full-length G and F proteins made as chimeric constructs with fluorescent proteins at their C-terminal tails. These chimeric constructs are expressed on the cell surface and show fusion activity comparable to wild-type proteins (fig. S3, A to E). Transfected cells are overlaid onto patterned SLBs consisting of 4-μm-diameter bilayer circles surrounded by polylysine–polyethylene glycol (PLL-PEG) borders (Fig. 2, A and B). The PLL-PEG is functionalized with arginine-glycine-aspartate (RGD) peptides that engage integrin on the surface of overlaid cells, inducing cell adhesion and spreading into a two-dimensional membrane interface. The circular bilayer patches are formed by 2% Ni-NTA DOGS in dioleoylphosphatidylcholine (DOPC), allowing the surface to be functionalized with His-tagged proteins, including ephrinB2 (Fig. 2A).

We overlaid live cells transfected with G–enhanced green fluorescent protein (eGFP) and F tagged with mScarlet-I (F-mSci) on the patterned substrates functionalized with AF647-labeled monomeric ephrinB2, allowing visualization of the proteins. Dense clusters of NiV G and ephrinB2 form specifically at the live cell–SLB interfaces that are localized to the circular bilayer patches (Fig. 2C and fig. S4, A and B). The clusters often appear as dynamic punctae (movie S4) and likely represent sites of localized contact of cellular plasma membrane extensions containing G with ephrinB2 on the SLB. No clustering of ephrinB2 is observed in the absence of transfected G (fig. S4C). No coclustering of NiV F was observed with NiV G–ephrinB2 clusters (Fig. 2C). While G was observed to concentrate in bilayer patches containing ephrinB2, F-mSci fluorescence remained diffusely distributed.

Based on the current models, NiV F was expected to form complexes with G in its nonactivated, prefusion state and dissociate from G upon activation (*3*, *47*, *48*). Therefore, the lack of coclustering of F with G after binding to ephrinB2 could be due to F activation and dissociation. To test this possibility, we used a disulfide-bond mutant of NiV F (N100C-A119C) that is locked in its prefusion conformation and cannot be activated (*49*). No coclustering of this mutant with NiV G was observed (Fig. 2D), indicating that locking in the prefusion form of F did not stabilize interactions with G.

Since ephrinB2 binding to G could induce conformational changes in G that also lead to F dissociation, we tested whether clustering of F using an anti-F prefusion-specific monoclonal antibody, 5B3 (*50*), might drive colocalization of F and G. We generated a single-chain Fv construct of 5B3 (scFv5B3) with a C-terminal His-tag to functionalize the SLBs. When cells are overlaid onto scFV5B3 bilayers, F-mSci becomes enriched in the circular bilayer areas. In contrast, NiV G does not cocluster with F and even appears to be excluded from the NiV F clusters in some cells (Fig. 2E). The structure of 5B3 bound to NiV F shows that it engages a quaternary epitope toward the midsection of the prefusion F head (*51*), which appears distinct from the surfaces of F that may interact with G. However, we cannot exclude the possibility that 5B3 blocks interactions with G. Nonetheless, the totality of the data indicates that ephrinB2:G complexes do not show any preferential interactions with F and we find no evidence of stable F-G complexes before activation.

### NiV F is activated, inserts into ephrinB2-functionalized SLBs, and causes lipid transfer

Previous SLB studies have established that single influenza virions exposed to low pH are able to progress to hemifusion and, in the case of cushioned SLBs, to full bilayer fusion, through HA-mediated insertion into the bilayer (*52*). Since NiV activation is triggered by receptor binding to G, we examined whether NiV F conformational changes and fusion activity are reconstituted in our live cell–SLB setup using two approaches: We monitored binding of an inhibitory HRB peptide that detects an activated F intermediate and we examined whether dye-labeled lipid could be transferred from the SLB to the cell membrane. The HRB peptide consists of the α-helical stalk region of prefusion NiV F, which forms a stable six-helix bundle with the HRA peptide region in the postfusion conformation of F (Fig. 3A) (*53*, *54*). Addition of synthetic HRB peptide inhibits fusion by trapping F at the prehairpin intermediate, after fusion peptides have inserted into the target cell membrane but before refolding to the postfusion conformation (Fig. 3A) (*29*, *55*).

We used AF647-labeled HRB peptide as a probe for F activation on NiV F–transfected cells overlaid on ephrinB2-functionalized patterned bilayers. Robust fluorescence indicative of HRB binding at the SLB-cell interface was readily detected using cells expressing wild-type F and G overlaid onto ephrinB2-functionalized substrates (Fig. 3B). Cells that were lacking F or that expressed the stabilized pre-F mutant N100-A119C did not show any significant HRB accumulation (Fig. 3B). We further quantified this difference by determining the per-pixel intensity histograms over the bilayer patches interacting over three cells (Fig. 3C). Consistent with the visual

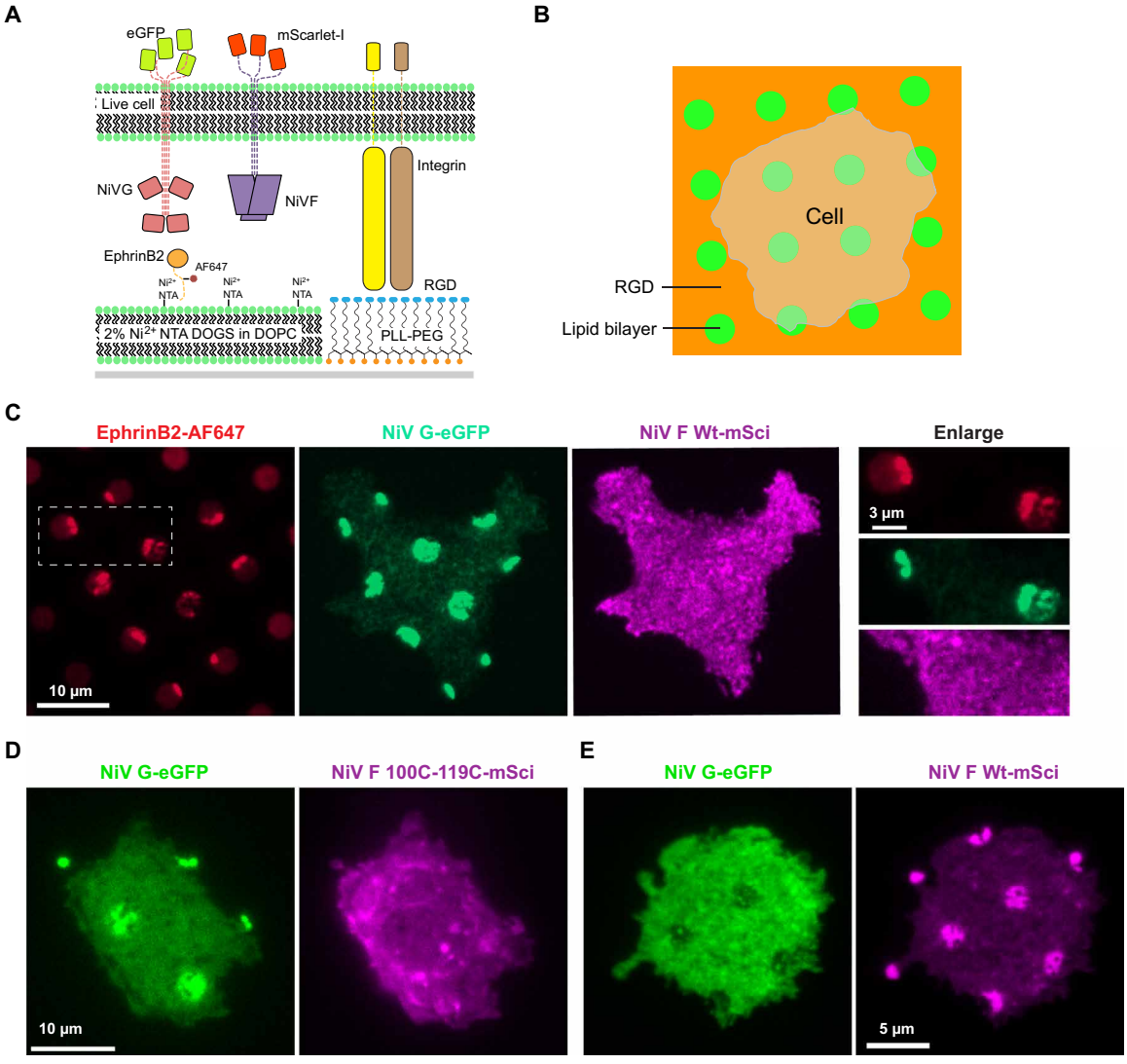


**Fig. 2. Investigation of NiV F–NiV G interaction.** (**A**) Experimental setup for overlay of full-length NiV G and NiV F cotransfected Chinese hamster ovary cells on patterned substrates. EphrinB2 ectodomain-functionalized SLB circles are arrayed between RGD-ligand functionalized PLL-PEG. (**B**) Schematic of patterned bilayer substrate. (**C**) Cellular distribution of NiV G–enhanced green fluorescent protein (eGFP) and NiV F Wt-mSci in cells overlaid on patterned ephrinB2-AF488–functionalized SLBs. (**D**) Cellular distribution of NiV G–eGFP and NiV F N100C-A119C-mSci in cells overlaid on patterned ephrinB2-AF488–functionalized SLBs. (**E**) Cellular distribution of NiV G–eGFP and NiV F Wt-mSci in cells overlaid on patterned scFv5B3–functionalized SLBs.

observations, these intensity histograms show that wild-type F, but not stabilized pre-F, concentrate AF647-labeled HRB peptide to the bilayer interface. Overall, these data show that F is activated by the reconstituted receptor substrate, with HRB assembling onto prehairpin F intermediates that expose the N-terminal HRA segments.

We also observed a distinct localization of the HRB-trapped, prehairpin F to the circular bilayer patches, which indicates that the activated F has become associated with the SLB, potentially through fusion peptide insertion. This localization is only detectable because of the use of the patterned substrate, in which functionalized bilayer patches are surrounded by PLL-PEG borders. The HRB localization is consistent with the sites of F activation being confined to the circular bilayer areas, which contain the activating ephrinB2 (Fig. 2, A and B). Furthermore, the confinement of the activated F proteins to the circular patches indicates that, once activated, the F trimers are unable to diffuse into the PLL-PEG regions. The PLL-PEG borders do not impede diffusion of proteins within the cellular plasma membrane but restrict lateral diffusion of SLB-associated proteins outside of the bilayer regions. We conclude that the combination of HRB binding and patch confinement indicates that the F prehairpin intermediate has likely inserted its fusion peptides into the SLB and is blocked from diffusing past the PLL-PEG barriers (Fig. 3D). As HRB binding can be observed in activated cells up to 2 hours following bilayer overlay (table S1), these intermediates may persist over long periods of time or may be replenished by newly synthesized F protein that is trafficked to the cell surface.

We further investigated whether F activation leads to lipid mixing between the SLB and overlaid cells. Prior single-particle studies of influenza virion fusion with SLBs relied on monitoring the dequenching of lipophilic dye in the virion, yielding a burst of fluorescence at the moment of HA-mediated fusion (*56*). In our setup, the volume of the cellular membrane precludes using this dequenching

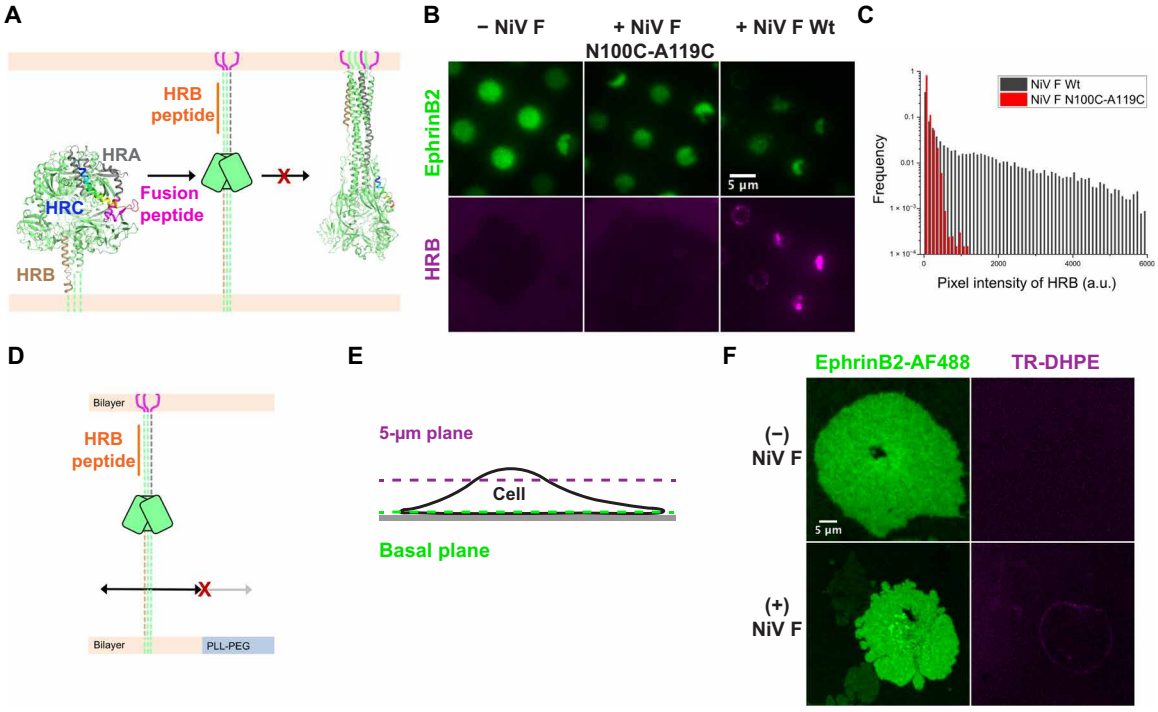


**Fig. 3. NiV F is activated at the live cell–SLB interface.** (**A**) Schematic of the F conformation from pre- to postfusion conformation showing HRB peptide trapping at the prehairpin intermediate. (**B**) Binding of HRB to regions of NiV G–ephrinB2 cluster-mediated NiV F activation. NiV $G_{full}$ Wt cells cotransfected with pCAGGS, NiV $F_{full}$ Wt, or NiV F N100C-A119C were overlaid on SLB functionalized with ephrinB2-AF488 in the presence of 5 μM HRB-AF647. (**C**) Pixel intensity profile of HRB-AF647 binding fluorescence averaged over three cells. (**D**) The F membrane–spanning prehairin intermediate is restricted from diffusing out of bilayer areas. (**E**) Schematic of the confocal scanning microscope illumination planes for observation of lipid mixing. (**F**) Reconstitution of lipid mixing on a live cell–continuous SLB setup. Confocal microscopy images in the ephrinB2-AF488 channel were taken at the plane of the bilayer to image the SLB and in TR-DHPE channel at 5 μm above plane of the bilayer to selectively image fluorescent dye transfer into the cell membrane. a.u., arbitrary units.

approach to measuring F activation. Instead, we investigated whether dye transfer from the SLB to the overlaid cell could be detected under fusion activating conditions. We loaded Texas Red–1,2-dihexadecanoyl-sn-glycero-3-phosphoethanolamine (DHPE) into a homogeneous SLB, overlaid it with transfected cells, and monitored transfer of the dye from the SLB to the cell using a confocal microscope, imaging the cellular membrane at a plane 5 μm above the glass slide and SLB (Fig. 3E). This allowed us to measure fluorescence from the cell membrane due to dye transfer events. We observed a ring of TR-DHPE fluorescence in overlaid cells only in the presence of NiV F, G, and ephrinB2, but not in the absence of F (Fig. 3F). Overall, these observations indicate that ephrinB2 presented on SLBs results in authentic reconstitution of the receptor-dependent activation of F and lipid mixing between the SLB and cell membrane.

## Single-particle tracking of NiV F in live cells reveals a trapped intermediate

Having established the reconstitution of F activation, we asked whether dynamic features of individual F trimers could reveal additional insights into its activated state(s). The molecular level behavior of F could not be resolved in bulk fluorescence imaging owing to the uniform distribution of F throughout the cell at high density. In contrast, single-particle tracking can capture transient interactions and heterogeneous behavior at the molecular level, and at high temporal resolution.

To track the behavior of single F trimers, we used a NiV F construct with a C-terminal Halotag fused after the cytoplasmic tail. This F construct was expressed on the cell surface and induced fusion comparably to wild-type F (fig. S3, F and G). Individual NiV F trimers in live cells were labeled with photoactivatable Janelia Fluor 646–Halo ligand (PA-JF646) and visualized after cells were overlaid onto SLBs. The observed particle diffusion behavior is heterogeneous, from highly mobile to effectively immobile particles (Fig. 4A). Displacements of F trimers over 50 ms were obtained by single-particle tracking analysis of videos collected under activating conditions in the presence of G and ephrinB2 (movie S5) and nonactivating conditions, where either G or ephrinB2 is absent (movies S6 and S7). An algorithm was developed to sort the particles and their displacements by their location inside or outside bilayer patches, where ephrinB2- and G-dependent activation could occur, using image masks (data S1). The distributions of the displacement step sizes inside the bilayer areas to those outside in the PLL-PEG borders provided a comparison for F particles within the same cell that are exposed to activating and nonactivating areas of the substrate.

Under nonactivating conditions, the diffusion behavior of single F particles is indistinguishable for molecules inside and outside the circular bilayer patches. These F step size distributions remain identical in cells expressing only F and overlaid onto ephrinB2 SLBs (Fig. 4B) and in cells expressing F and G overlaid onto SLBs lacking ephrinB2 (Fig. 4C).

In contrast, when cells expressing F and G are overlaid onto SLBs functionalized with ephrinB2, a pronounced and reproducible shift toward smaller F step sizes inside the bilayers is observed (Fig. 4, D and E, and fig. S5, A and B). A difference plot of the inside versus outside step size distributions shows a distinct loss of particles

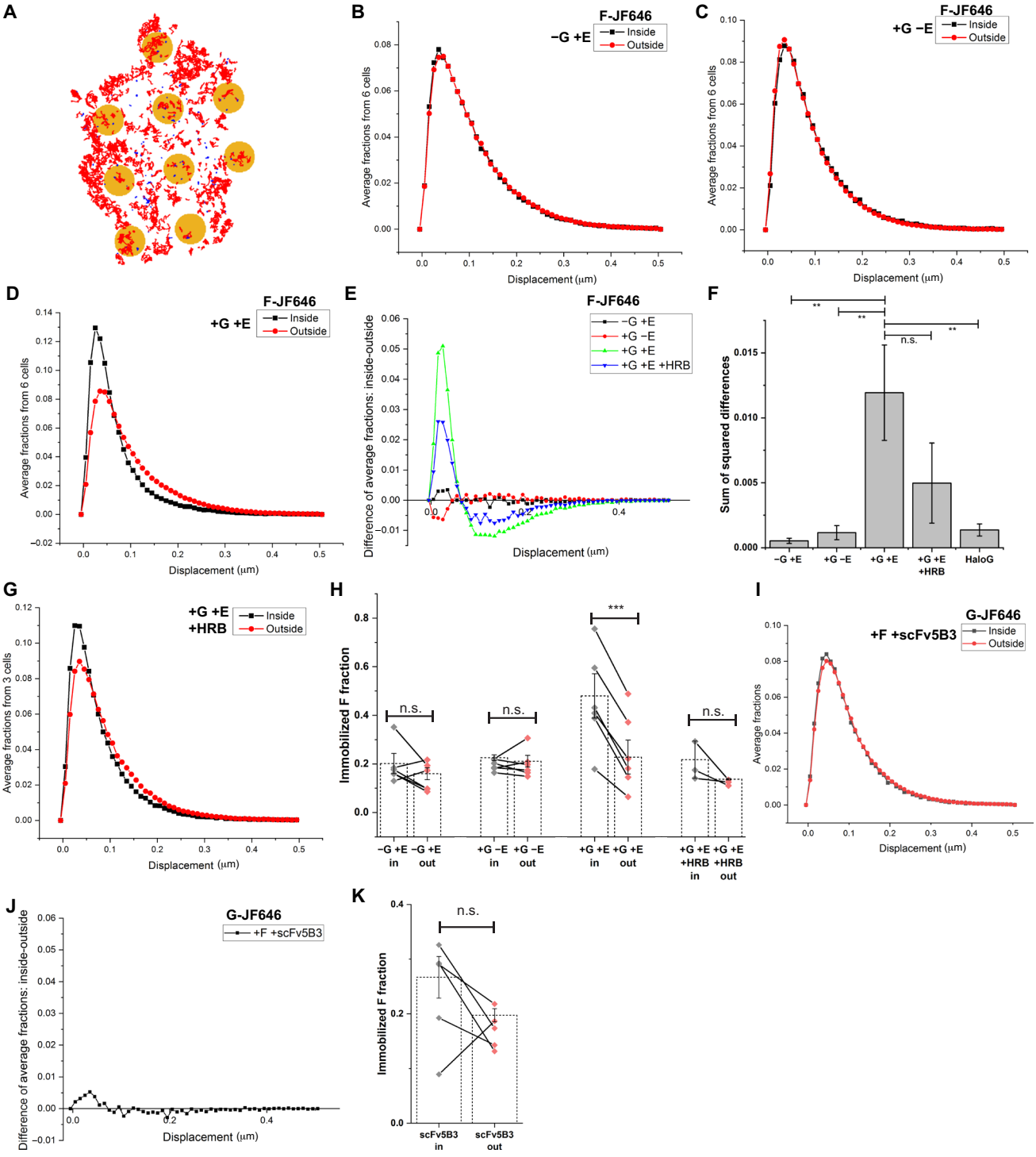


**Fig. 4. NiV F is immobilized upon activation by NiV G and ephrinB2.** (**A**) Overlay of F-Halo-JF646 tracks, spots, and bilayer areas. Red tracks = mobile; blue tracks = immobile. (**B**) Displacement distributions of F-Halo-JF646 in F-Halo cells with ephrinB2-functionalized bilayers. (**C**) Displacement distributions of F-Halo-JF646 in F-Halo/$G_{full}$-Wt cells with nonfunctionalized bilayers. (**D**) Displacement distributions of F-Halo-JF646 in F-Halo/$G_{full}$-Wt cells with ephrinB2-functionalized bilayers. (**E**) Difference of average displacement fractions (inside versus outside) from F-Halo-JF646 tracking. (**F**) Averaged sum of squared differences of F-Halo-JF646 or G-Halo-JF646 step size distributions. $n = 6$ for −G +E, +G −E, and +G +E. $n = 3$ for +E +G +HRB. $n = 5$ for G-Halo. $P$ values from one-way analysis of variance (ANOVA) followed by Dunnett's T3 test, compared to G-Wt/F-Wt control. (**G**) Displacement distributions of F-Halo in F-Halo/$G_{full}$-Wt cells with ephrinB2-functionalized bilayers and HRB. (**H**) Fraction of immobilized particles inside and outside bilayer regions for (A) to (D). (**I**) Displacement distributions of G-Halo in G-Halo/NiV $F_{full}$-Wt cells with ephrinB2-functionalized bilayers. (**J**) Difference of average displacement fractions (inside versus outside) from G Halo-JF646 tracking. (**K**) Fraction of immobilized G-Halo-JF646 particles inside and outside bilayer regions functionalized with scFv5B3. For (H) and (K), $P$ values were determined by paired-value $t$ test of the immobilized fraction of particles within the same cell. n.s., not significant, $^{**}P < 0.01$, $^{***}P < 0.001$.

with larger diffusion steps and significant enrichment of particles with limited mobility (Fig. 4E). The sum of the squared differences between inside and outside over the entire distribution shows a significant change in the overall F behavior only under activating conditions (Fig. 4F). These data indicate that within the activating circular regions of the patterned lipid bilayer, F particles are specifically altered in a manner that reduces their diffusion rates. We hypothesized that the reduced diffusion of F might be explained by the formation of the activated F prehairpin intermediate, since it inserts its hydrophobic peptides into the SLB and would thereby anchor F in two membranes. We further hypothesized that the addition of inhibitory HRB peptides would stabilize the prehairpin intermediate and potentially result in further enrichment of the slowly diffusing F particles. To our surprise, the addition of HRB peptide had the opposite effect on F diffusion, significantly blocking the shift to smaller step sizes (Fig. 4, E to G; fig. S5, A and B; and movie S8). These data indicate that the reduction in F diffusion after activation is not caused by the insertion of the prehairpin F intermediates into the SLB. We believe that the slow-diffusing F represents a novel, distinct intermediate along the F membrane fusion pathway, as will be discussed below in more detail.

We suspected that the downward shift in F displacement step sizes could be due to increased particle immobilization rather than simply slower diffusion rate, as immobile particles were clearly visible in track overlays (Fig. 4A and movie S9). We developed an algorithm to sort the locations of entire tracks by whether they spent all of their lifetime inside or outside the bilayer areas or spent part of their time in both domains of the patterned substrate (data S2). We then determined whether each particle is immobilized on the basis of whether their mean squared displacement over time reduces to a constant that is below an empirically determined noise threshold for NiV F particles in our cell setup (data S3). This analysis indicates that there is a significant enrichment of immobilized F particles in the population that exclusively reside inside bilayer areas compared to those that reside exclusively outside, but only when both NiV G and ephrinB2 are present. Addition of HRB reduces the difference in the immobilized fraction to less than significant levels (Fig. 4H), consistent with the inhibition observed in the step size distribution analysis. Overall, these single-molecule observations of F diffusion support the conclusion that activated F trimers become immobilized after exposure of the internal HRA domains and independently of fusion peptide insertion into the SLB.

We conducted a converse experiment in which NiV G with a C-terminal Halo tag was labeled with PA-JF646, to examine whether single-particle tracking could more sensitively detect F-G interactions. G was tracked in cells expressing F that were overlaid onto scFv5B3-functionalized patterned bilayers, similar to the bulk fluorescence measurements conducted above. In this case, no shift in the displacement distribution of G was observed (Fig. 4, I and J). NiV G Halo on NiV F–transfected cells also does not have a significantly greater fraction of immobilized particles inside bilayer areas when overlaid on scFv5B3 functionalized patterned bilayers (Fig. 4K). These data further indicate that any pre–F-G assemblies are likely weak and transient, given the caveat that 5B3 could potentially block these interactions.

### G-dependent clustering of ephrinB2 is essential for F activation

Receptor-induced oligomerization of viral glycoproteins has been hypothesized to play a role in paramyxovirus fusion activation (*26*, *30*) but has been experimentally difficult to examine quantitatively. To determine whether ephrinB2 clustering is essential for F activation, we designed a substrate surface that immobilized isolated ephrinB2 monomers on the glass slide. In this setup, Ni-NTA-PEG is attached to the glass surface and surrounded by a lipid bilayer field containing no Ni-NTA headgroups. EphrinB2 is bound to the immobilized Ni-NTA-PEG, which prevents the lateral diffusion and clustering of the receptor (Fig. 5A). The surrounding lipid bilayer should allow NiV F fusion peptide insertion and enable the detection of F activation by HRB binding. A parallel control substrate was set up with NTA-PEG–lacking nickel, surrounded by a lipid bilayer containing Ni-NTA lipid. EphrinB2 captured through these lipids would be unrestrained in its lateral diffusion and allow receptor clustering (Fig. 5A). For these two substrates, labeled ephrinB2 capture densities were set to similar levels, as measured by average AF488 fluorescence, and overlaid with NiV G– and F–mCherry–expressing cells. Cells overlaid onto ephrinB2 bound to Ni-NTA-PEG showed no F activation (Fig. 5B). In contrast, when ephrinB2 is captured through Ni-NTA lipids, F showed robust activation (20 of 30 cells), as observed by HRB-AF647 accumulation in the cell:bilayer interface (Fig. 5B). By restricting the ability of ephrinB2 to cluster, we show that NiV F activation is dependent on the ability of ephrinB2 to form higher-order oligomers with NiV G.

We explored whether cytoskeletal forces could contribute to the clustering of ephrinB2 on SLBs and thereby lead to F activation using the actin polymerization inhibitor Latrunculin A. In the presence of Latrunculin A, we observe that F no longer binds HRB-AF647 on DOPC substrates, consistent with a role for the cellular cytoskeleton in the F activation step (Fig. 5C). In the presence of blebbistatin, an inhibitor of myosin, F activation is enhanced (Fig. 5D). However, clustering of ephrinB2 and NiV G still occurs, indicating that cytoskeleton activity is not required for clustering and instead plays an additional role in fusion activation that is not yet defined.

We also explored whether the fluidity of the SLB might affect ephrinB2 clustering and F activation. DOPC exists in a fluid phase at 37°C, facilitating lateral diffusion and clustering of ephrinB2 on the SLB. We prepared membranes with 1,2-dipalmitoyl-sn-glycero-3-phosphocholine (DPPC), which is in the gel phase at 37°C, leading to reduced lateral mobility of the lipid-associated ephrinB2 (*57*). Previous studies of the formation of E-cadherin junctions have demonstrated that they only form efficiently on membranes of limited mobility with a dependence on actomyosin-driven processes (*57*). SLBs prepared with DPPC and functionalized with ephrinB2-AF488 still show clustering of ephrinB2 and NiV F activation (fig. S6).

## DISCUSSION

Here we have reconstituted and characterized initial steps in the activation of the multicomponent NiV membrane fusion machinery using SLB:live cell TIRF microscopy. We have used single-particle tracking experiments to investigate interactions of the NiV F and G proteins, as purified ectodomains and within live cells. This has allowed us to directly observe changes in diffusion behavior of activated F intermediates along the membrane fusion pathway. Our data support the following conclusions: (i) NiV F and G ectodomains do not interact with any measurable affinity, despite a need to coordinate their respective roles in receptor binding and bilayer fusion. (ii) In cells, the full-length F and G proteins also do not show stable interactions, either before or after ephrinB2 activation.

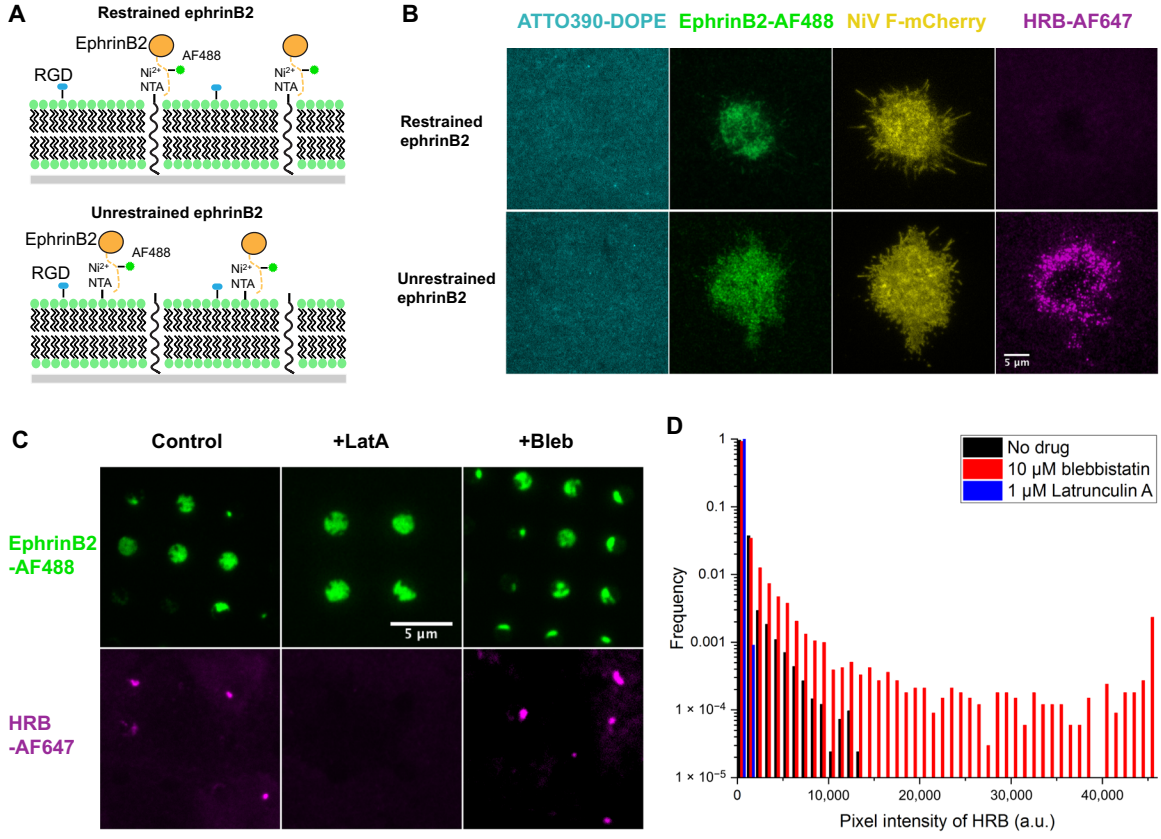


**Fig. 5. Clustering of ephrinB2 and the actin cytoskeleton is necessary for F activation.** (**A**) Schematic of restrained (top) and unrestrained ephrinB2 (bottom) on the SLB. Restrained ephrinB2 is anchored through Ni-NTA-PEG linkers attached to the glass slide, preventing lateral diffusion. Unrestrained ephrinB2 is captured through Ni-NTA lipid that surrounds uncharged Ni-free NTA-PEG. (**B**) Restrained ephrinB2 does not allow for F activation, as monitored by HRB-AF647 binding (top). In contrast, unrestrained ephrinB2 captured at comparable overall densities (as measured by AF488 fluorescence) leads to activation of F (bottom). (**C**) Binding of HRB-AF647 to NiV $F_{full}$ Wt in bilayer areas with ephrinB2-AF488 bound to 4% Ni-NTA-DOGS in the presence of Latrunculin A or blebbistatin. (**D**) Pixel intensity profile of HRB-AF647 binding fluorescence averaged over nine cells in the presence or absence of blebbistatin.

(iii) Reconstitution of the ephrinB2 ectodomain onto purified lipid substrates is sufficient for F activation. (iv) Activated F inserts into the SLB and mediates lipid transfer to cells. (v) Activated F becomes immobilized, but this immobilization is suppressed by trapping the F prehairpin intermediate. (vi) NiV fusion requires ephrinB2 clustering to activate F-mediated fusion in a manner that can depend on the actin cytoskeleton.

In the current models of henipavirus activation, the F and G proteins have been proposed to interact more strongly before activation and dissociate after activation (*3*, *47*, *48*). Our current findings show no evidence of stable F-G complexes occurring on the cell surface before ephrinB2 activation. We did not detect any interaction between the F and G ectodomains (Fig. 1L). We also did not detect any interaction between full-length proteins, as we observed no colocalization of NiV G and F under nonactivating conditions (Fig. 3, D and E) and no shift in the displacement distributions of NiV G (Fig. 4K) inside bilayer areas that contain anti-F scFv–NiV F clusters. Our observations are consistent with a super-resolution microscopy study of F and G expressed on the cell surface, where no colocalization above random levels was observed (*37*). Under activating conditions, we see no coclustering of NiV F with NiV G–ephrinB2 punctae (Fig. 2C). Upon activation, we observe a significant increase in the percentage of the F molecules (~21%) that become immobilized inside the bilayer areas where NiV G–ephrinB2 clusters reside (Fig. 4H). However, this immobilization does not lead to a concentration of bulk F with ephrinB2:G punctae, indicating that immobilized particles are more evenly distributed throughout the bilayer patch. Together, these data support a revision of the henipavirus fusion model in which F-G interactions are more transient and dynamic both before and after ephrinB2 receptor engagement.

Under activating conditions, we readily observe fluorescent HRB peptide binding to the cell:SLB interface (Fig. 3, B and C), indicative of substantial numbers of F molecules adopting a prehairpin intermediate and inserting their fusion peptides into the SLB (Fig. 3A). F activation leads to lipid dye transfer (Fig. 3F) as well as F immobilization, and this immobilization is inhibited by HRB binding (Fig. 4H). We believe that this experimental setup allows us to study activated intermediates along the fusion pathway up to a hemifusion stage and that the SLB system prolongs the lifetime of the F prehairpin intermediate when HRB is added. This conclusion is supported by the following observations: (i) AF647-HRB binding shows strong and robust accumulation at the bilayer interface, indicating a significant accumulation of the prehairpin state (Fig. 3, B and C). (ii) AF647-HRB binding is observed up to 2 hours after overlaying cells on activating substrates, indicating a persistence of the prehairpin state, a persistence of F activation, or both (table S1). (iii) Prior studies of influenza virus fusion have established that

SLBs enable progression to a hemifusion state, whereas full fusion requires using PEG- or dextran-cushioned bilayers (*52*). We hypothesize that these conditions could contribute to F immobilization by three potential mechanisms, which could all be blocked by exogenous HRB inhibitor addition: First, activated prehairpin F molecules could self-oligomerize through interactions that depend on the flexibility and/or exposure of the internal HRA region (Fig. 6A). Second, prehairpin F trimers could form extensive interactions between the HRA domains and lipid bilayer surfaces that could restrict diffusion (Fig. 6A). Third, flexible prehairpin or potentially postfusion F trimers could be sequestered at sites of hemifusion stalk formation that cannot resolve to full membrane merger and pore expansion (Fig. 6A). We cannot exclude the possibility that immobilized F trimers have refolded to the postfusion 6HB conformation, but the diffusion of the postfusion form within the plasma membrane would not be expected to differ so significantly from the prefusion trimer. We therefore conclude that the immobilized F represents a state of F that is either a structural intermediate preceding 6HB formation or a postfusion form that is entrapped in hemifusion intermediates. Trapped fusion intermediates may consist of nascent fusion pores formed by the cooperative action of multiple F trimers, which has been proposed due to changes in membrane fusion outcomes with different F and attachment protein densities (*58*, *59*) and from the derivation of the number of independent events during influenza virion fusion (*56*, *60*). Further studies on the F protein stoichiometry, conformational state, and membrane topology of these immobile F particles will be necessary to resolve these hypotheses.

Our immobilized ephrinB2 substrate shows that clustering of ephrinB2 caused by the binding of NiV G is essential for activation of F fusion (Fig. 5B). To our knowledge, this is the first experimental setup where host receptor mobility has been systematically altered to test its role in viral fusion activation. In addition, we show that F activation is dependent on actin polymerization. We demonstrated that cluster formation and fusion activation still occurs when cells are overlaid on ephrinB2-functionalized bilayers of DOPC, but is inhibited by Latrunculin A, an actin polymerization inhibitor, and enhanced by blebbistatin, a myosin II inhibitor (Fig. 5, C and D). The actin cytoskeleton has been shown in a previous study to play a role in cell-cell fusion mediated by PIV5 glycoproteins (*61*). Paramyxovirus fusion and attachment proteins are not known to bind to actin, myosin, or other cytoskeletal components, so the cytoskeleton may be exerting its effect indirectly on the proteins by some degree of force generation and/or remodeling of the cell environment surrounding the viral glycoproteins.

These observations indicate that there is likely a threshold level of ephrinB2 oligomerization needed to yield robust F activation. In one scenario, a "tetramerization" model, ephrinB2 tetramers may be needed to simultaneously engage the four receptor-binding domains of individual G proteins to fully activate individual G tetramers (Fig. 6B). In another scenario, larger clusters of ephrinB2:G complexes may be needed to recruit and activate prefusion F (Fig. 6C). This type of threshold clustering, in addition to stalk exposure, could provide a key barrier to F activation that ensures that it occurs at the right time and place. Clustering of G may also overcome the apparent low-affinity interactions underlying F and G interactions. While clustering of paramyxovirus fusion proteins has been proposed to play a role in fusion activation, our approaches provide a route to quantitative investigations. We do not observe a persistent interaction of prehairpin F with G punctae, which would be predicted for a model in which G "chaperones" F through its conformational changes. However, we note that HRB-trapped prehairpin F does more often show some apparent colocalization with G punctae, although videos demonstrate that these colocalizations are dynamic and transient.

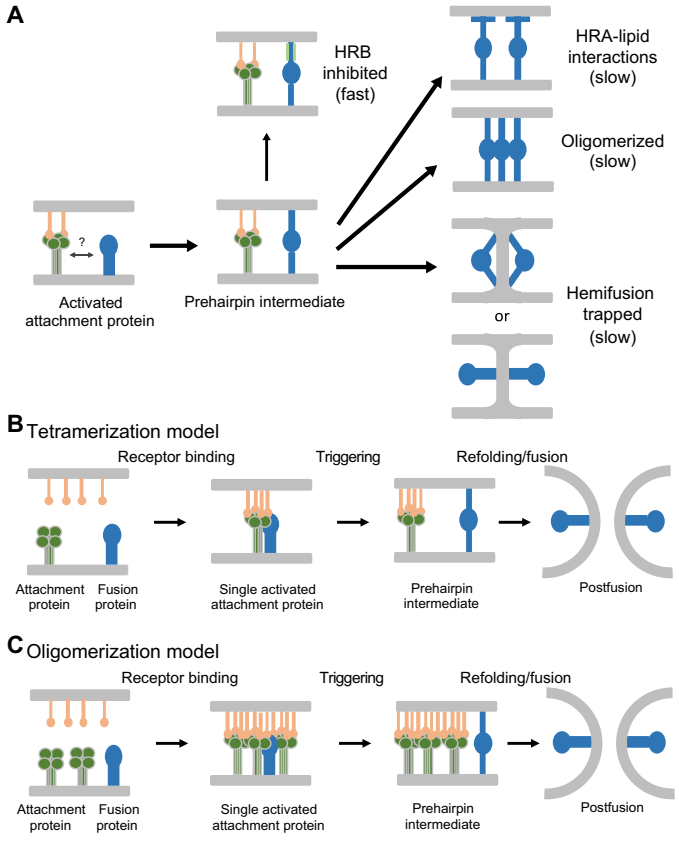


**Fig. 6. Models for F immobilization and membrane fusion activation.** (**A**) Following activation, F forms a fast-diffusing prehairpin intermediate when trapped by HRB peptide binding. Without HRB peptide inhibition, F forms a slow-diffusing state that could be due to higher-order F oligomerization via HRA domains or trapping at hemifusion stalks. (**B**) Schematic for an ephrinB2 tetramerization model for NiV G and F activation. (**C**) Schematic for an oligomerization model requiring clustering of ephrinB2:G complexes to activate F.

In summary, we propose an overall revised model for the henipavirus fusion mechanism based on our observations. In this model, F and G do not form stable complexes, but likely dynamically sample low-affinity interactions in their prefusion states. Contact between NiV G and ephrinB2 oligomerizes receptor, leading to a threshold cluster of ephrinB2:G needed for F activation. F activation leads to an intermediate state with reduced mobility, either through lateral protein interactions or interactions with lipids at the dual bilayer interface, which may contribute to the coordination of pore formation and opening. While our studies of this mechanism are most analogous to in vivo cell:cell fusion, we anticipate that essential features also apply to the triggering of viral particle entry. Last, we anticipate that the SLB:live cell methodologies that we have developed here will be useful for studying the mechanisms and inhibition of other multicomponent viral fusion mechanisms found in other paramyxoviruses and herpesviruses.

## MATERIALS AND METHODS

### Plasmid constructs

A codon-optimized DNA fragment containing the gp64 signal peptide, NiV F residues 26 to 482, GCN4 trimerization domain (*5*, *49*), factor XA cleavage site, and His8-tag was obtained by gene synthesis and cloned into the Eco RI and Nhe I sites of pCAGGS3 to make NiV $F_{ecto}$. NiV $G_{ecto}$ with an extended linker (Wt 40 Å) was made by digesting the NiV $G_{ecto}$-Wt in pENTR1A plasmid (*41*) with Sal I and Cla I. The intervening fragment was replaced by Gibson assembly with a fragment consisting of the gp64 signal peptide, His6-tag, enterokinase cleavage site, an additional linker sequence, and NiV G coding sequences and overlapping sequences with the vector fragment for assembly. The linker sequence KLGVSSSEVSNVEADSAA was chosen using SynLinker (*62*) with the criteria of being as long as the estimated height of the GCN trimerization domain of the NiV $F_{ecto}$ construct (~40 Å) used to stabilize it in the prefusion conformation. To make NiV $G_{ecto}$-Wt-40 Å-amber, the linker sequence was modified to KLGVSSSE*SNVEADSAA where * is the stop codon TAG using the Q5 site-directed mutagenesis kit (New England Biolabs) with the primers NiVGect_40AlinkAmber_For and NiVGect_40AlinkAmber_Rev. The NiV $G_{ecto}$ Wt 40 Å-amber gene was transferred from pENTR1A to pcdnaDEST40 by LR Clonase II Gateway cloning (Life Technologies) for expression.

NiV $G_{ecto}$ L181A-40 Å was made by digesting the NiV $G_{ecto}$ L181A in pENTR1A plasmid (*41*) with Sal I and Cla I. The intervening fragment was replaced by Gibson assembly with a fragment consisting of the gp64 signal peptide, His6-tag, enterokinase cleavage site, the linker sequence KLGVSSSEVSNVEADSAA, and NiV G coding sequences and overlapping sequences with the vector fragment for assembly. NiV $G_{ecto}$ L181A-40 Å-amber was made by digesting the NiV $G_{ecto}$ L181A in pENTR1A plasmid (*41*) with Sal I and Cla I. The intervening fragment was replaced with that of NiV $G_{ecto}$ Wt-40 Å-amber resulting from Sal I and Cla I digestion.

NiV $G_{ecto}$ V182A-40 Å was made using the Q5 site-directed mutagenesis kit (New England Biolabs) with the primers NiVGect_V182A_Q5_For and NiVGect_V182A_Q5_Rev with NiV $G_{ecto}$ Wt-40 Å in pENTR1A plasmid as the template. NiV $G_{ecto}$ V182A-40 Å-amber was made by Q5 site-directed mutagenesis kit (New England Biolabs) with the primers NiVGect_V182A_Q5_For and NiVGect_V182A_Q5_Rev with NiV Gecto Wt-40 Å-amber in pENTR1A plasmid as the template.

EphrinB2-Fc-mNG was made by amplifying the mNeonGreen gene from pNCS-mNeonGreen (Allele Biosciences) with the primers mNeonGreen_For and mNeonGreen_Rev, digesting the resulting fragment and the NiV $F_{ecto}$ pCAGGS3 plasmid with Kpn I and Nhe I, and ligating the mNeonGreen fragment and pCAGGS3 vector fragment with T4 ligase. The ephrinB2-Fc fragment from the ephrinB2-Fc-pTT5 plasmid (*41*) was amplified with the primers pTT5_EcoRI_For and IgG1-Fc_splitlink_Rev and digested with Eco RI and Kpn I. The ephrinB2-167 fragment from the S-tag-ephrinB2-167-pTT5 plasmid (*41*) was amplified with the primers pTT5_EcoRI_For and EphB2-167_splitlink_Rev and digested with Eco RI and Kpn I. The digested ephrinB2 construct fragments were ligated with the mNeonGreen-pCAGGS3 plasmid digested with Eco RI and Kpn I.

The His8-ephrinB2-229 fragment was amplified with the primers pTT5_EcoRI_For and EphB2-229-XA-His8_Rev from the ephrinB2-Fc-pTT5 plasmid and digested with Eco RI and Nhe I. This was ligated with the vector fragment from NiV $F_{ecto}$ pCAGGS3 digested with Eco RI and Nhe I.

A codon-optimized DNA fragment containing scFv1023 was digested with Hind III and Not I and ligated with the Hind III– and Not I–digested vector fragment of pTT5 (National Research Council of Canada). A codon-optimized DNA fragment containing scFv5B3 was digested with Eco RI and Nhe I and ligated with the Eco RI– and Nhe I–digested vector fragment of pCAGGS.

NiV G–eGFP in pCAGGS was constructed by Gibson Assembly of the DNA fragments eGFP, NiV G-KpnI640, and the vector-containing fragment of the NiV $G_{full}$-pCAGGS plasmid (gift from R. Lamb) digested with Sac I and Kpn I. The eGFP fragment was amplified with the primers pCG_SacI_mNG_For and mNG_GSlink_NiVGfull_Rev from the plasmid peGFP-C1 (Clontech). The NiV G fragment was amplified with the primers NiVGfull_Nterm_For and NiVGfull_KpnI640_Rev from the NiV $G_{full}$-pCAGGS plasmid.

NiV F-Wt-mSci in pCAGGS was constructed by Gibson Assembly of the DNA fragments NiV F-EcoRV-Cterm, mScarlet-I, and vector-containing fragment of the plasmid NiV $F_{full}$-pCAGGS (gift from R. Lamb) digested with Eco RV and Nhe I. The NiV F fragment was amplified with the primers NiVFfull_EcoRV_For and NiVFfull_Cterm_Rev from the NiV $F_{full}$-pCAGGS plasmid. The mScarlet-I fragment was amplified with the primers NiVFfull_link_CyOFP_For and mScarlet-I_pCG_Gib_Rev from the pmScarlet-i_C1 plasmid (gift from D. Gadella; Addgene plasmid no. 85044; http://n2t.net/addgene:85044; RRID:Addgene_85044).

NiV F N100C-A119C-mSci in pCAGGS was constructed in multiple steps. 119C-N was amplified from NiV $F_{full}$-mSci in pTT5 with the primers pTT5_EcoRI_For and NiVfull_119C_Rev, and 119C-mSci-C was amplified from NiV $F_{full}$-mSci in pTT5 with the primers NiVFfull_110C_119C_For and pTT5_NotI_Rev. NiV F A119C-mSci was made by overlap extension polymerase chain reaction (PCR) of the DNA fragments 119C-N and 119C-mSci-C with the primers pTT5_EcoRI_For and pTT5_NotI_Rev. The NiV F A119C-mSci fragment and the plasmid pTT5 were digested with Eco RI and Nhe I and ligated with T4 ligase. 110C-N was amplified from NiV F A119C-mSci in pTT5 with the primers pTT5_EcoRI_For and NiVfull_100C-119C_Rev, and 110C-mSci-C was amplified from NiV F A119C-mSci in pTT5 with the primers NiVFfull_110C_For and pTT5_NotI_Rev. NiV F N100C-A119C-mSci was made by overlap extension PCR of the DNA fragments 110C-N and 110C-mSci-C with the primers pTT5_EcoRI_For and pTT5_NotI_Rev. The NiV F N100C-A119C-mSci fragment and the plasmid pCAGGS were digested with Eco RI and Nhe I and ligated with T4 ligase.

NiV F N100C-A119C in pCAGGS was constructed similarly to NiV F N100C-A119C-mSci in pCAGGS. 119C-C was amplified from NiV $F_{full}$ in pTT5 with the primers NiVFfull_110C_119C_For and pTT5_NotI_Rev. NiV F A119C was made by overlap extension PCR of the DNA fragments 119C-N and 119C-C with the primers pTT5_EcoRI_For and pTT5_NotI_Rev. The NiV F A119C fragment and the plasmid pTT5 were digested with Eco RI and Nhe I and ligated with T4 ligase. 110C-C was amplified from NiV F A119C-C in pTT5 with the primers NiVFfull_110C_For and pTT5_NotI_Rev. NiV F N100C-A119C was made by overlap extension PCR of the DNA fragments 110C-N and 110C-C with the primers pTT5_EcoRI_For and pTT5_NotI_Rev. The NiV F N100C-A119C fragment and the plasmid pCAGGS were digested with Eco RI and Nhe I and ligated with T4 ligase.

NiV F-Halo in pCAGGS was constructed by Gibson Assembly of the DNA fragments NiV F-EcoRV-Cterm, Flink-Halotag, and

vector-containing fragment of the plasmid NiV $F_{full}$-pCAGGS (gift from R. Lamb) digested with Eco RV and Nhe I. The Flink-Halotag fragment was amplified with the primers NiVFfull-link-Halo_For and Halo_pCG_Rev from the pENTR4-Halotag plasmid (gift from S. Saurabh, Lucy Shapiro laboratory).

NiV G-Halo in pCAGGS was constructed by Gibson Assembly of the DNA fragments NiVG-KpnI640, Halotag-Glink, and vector-containing fragment of the plasmid NiV $G_{full}$-pCAGGS (gift from R. Lamb) digested with Sac I and Kpn I. The Halotag-Glink fragment was amplified with the primers pCG-SacI-Halo_For and Halotag-GSlink-NiVGfull_Rev from the pENTR4-Halotag plasmid (gift from S. Saurabh, Lucy Shapiro laboratory).

NiV F-mCh in pCAGGS was constructed by Gibson Assembly of the DNA fragments NiV F-EcoRV-Cterm, mCherry, and vector-containing fragment of the plasmid NiV $F_{full}$-pCAGGS (gift from R. Lamb) digested with Eco RV and Nhe I. The mCherry fragment was amplified with the primers NiVFfull_link_CyOFP_For and mScarlet-I_pCG_Gib_Rev from the pmCherry-C1 (Clontech) plasmid.

### Protein expression and purification

NiV $F_{ecto}$ in pCAGGS3 was transiently transfected into human embryonic kidney (HEK) 293F cells according to a high-density protocol described in (*63*). Cell culture medium was harvested 5 days after transfection and dialyzed with 25 mM sodium phosphate (pH 7.6), 200 mM NaCl, and 10 mM imidazole. NiV G was purified from the medium by Ni-NTA chromatography and eluted with a stepwise imidazole gradient. The peak fractions were further purified by size exclusion on a Superdex S200 column with 25 mM Hepes (pH 8.0), 200 mM NaCl, and 100 mM imidazole.

NiV $G_{ecto}$ Wt 40 Å, NiV $G_{ecto}$ L181A-40 Å, and NiV $G_{ecto}$ V182A-40 Å in pcdnaDEST40 were transiently transfected into HEK 293F cells according to a high-density protocol described in (*63*). NiV $G_{ecto}$ L181A-40 Å was expressed at 33°C instead of 37°C to improve protein assembly. NiV $G_{ecto}$ V182A-40 Å was transfected with one-fourth of the amount of DNA and polyethylenimine (PEI) to improve protein assembly. Cell culture medium was harvested 5 days after transfection and dialyzed with 25 mM sodium phosphate (pH 7.6), 200 mM NaCl, and 10 mM imidazole. NiV G was purified from the medium by Ni-NTA chromatography and eluted with a stepwise imidazole gradient. The peak fractions were further purified by size exclusion on a Superdex S200 column with 50 mM Hepes (pH 7.5), 150 mM NaCl.

NiV $G_{ecto}$-Wt-40 Å-amber, NiV $G_{ecto}$ L181A-40 Å-amber, and NiV $G_{ecto}$ V182A-40 Å-amber in pcdnaDEST40 were transiently transfected into HEK 293F cells according to a high-density protocol described in (*63*) with the following modifications based on the protocol for unnatural amino acid incorporation described in (*64*). A total of 1.6 mg of total plasmid DNA per liter of final cell culture with a 3:10:3 ratio of the plasmids TPS192, Bst-Yam, and NiV $G_{ecto}$-Wt-40 Å-amber was added to cells at high density. PEI (1 mg/ml) was added to a 2:1 PEI:DNA ratio. The DNA, cells, and PEI were incubated in the 37°C $CO_2$ shaker for 3 hours, followed by addition of FreeStyle medium supplemented with 1 mM p-azido-phenylalanine (pAzF) (Chem-Impex). The cell culture medium was harvested 5 days after transfection and dialyzed with 25 mM sodium phosphate (pH 7.6), 200 mM NaCl, and 5 mM imidazole. The NiV $G_{ecto}$-40 Å-pAzF proteins were purified from the medium by Talon bead chromatography and eluted with a stepwise imidazole gradient. The peak fractions were further purified by size exclusion on a Superdex S200 column with 50 mM Hepes (pH 7.5) and 150 mM NaCl.

All ephrinB2 construct plasmids were transiently transfected into HEK 293F cells according to a high-density protocol described in (*63*) and allowed to express for 5 days. EphrinB2-Fc-mNG was purified from the medium by Protein A chromatography and eluted with 25 mM MES (pH 6.6) and 3.6 M $MgCl_2$. EphrinB2-167-mNG was purified from the medium by Protein S chromatography and eluted with 100 mM tris (pH 7.5) and 3.0 M $MgSO_4$. EphrinB2-229-His8 was purified from the medium by Ni-NTA chromatography and eluted with a stepwise imidazole gradient. All constructs were further purified by size exclusion on a Superdex S200 column with 50 mM Hepes (pH 7.5) and 150 mM NaCl.

NiV $G_{ecto}$, ephrinB2-229, and ephrinB2-Fc were expressed and purified as described in (*41*). scFv1023 in pTT5 and scFv5B3 in pCAGGS were transiently transfected into HEK 293F cells according to a high-density protocol described in (*63*). Cell culture medium was harvested 5 days after transfection and dialyzed with 25 mM sodium phosphate (pH 7.6), 200 mM NaCl, and 10 mM imidazole. scFv was purified from the medium by Ni-NTA chromatography and eluted with a stepwise imidazole gradient. The peak fractions were further purified by size exclusion on a Superdex S200 column with 50 mM Hepes (pH 7.5) and 150 mM NaCl.

### Fluorophore labeling of proteins

Four to seven micromolar solutions of NiV $G_{ecto}$-40 Å-pAzF proteins were labeled with Click-iT DIBO-AF647 (Invitrogen) at a 2:1 dye:protein ratio. The dye and protein were incubated in 50 mM Hepes (pH 7.5) and 150 mM NaCl for 2 hours at room temperature. Ninety-five micromolar solutions of His8-ephrinB2-229 were labeled with *N*-hydroxysuccinimide (NHS) ester-Alexa Fluor 488 or NHS ester-AF647 (Thermo Fisher Scientific) at a 2:1 dye:protein ratio. The dye and protein were incubated in 50 mM Hepes (pH 7.5) and 150 mM NaCl for 1 hour at room temperature. A 23 μM solution of scFv5B3 was labeled with NHS ester-Alexa Fluor 488 (Thermo Fisher Scientific) at a 3:1 dye:protein ratio. The dye and protein were incubated in 50 mM Hepes (pH 7.5) and 150 mM NaCl for 1 hour at room temperature. Unbound dye was removed from all labeling reactions and buffer was exchanged to 50 mM tris (pH 7.5) and 150 mM NaCl with 0.5 ml of Zeba Spin 7 K molecular weight cut-off (MWCO) desalting columns (Thermo Fisher Scientific).

### HRB peptide

HRB peptides were synthesized by LifeTein. Unlabeled HRB peptide has the sequence VFTDKVDISSQISSMNQSLQQSKDYIKEAQRLLDTV with N-terminal acetylation and C-terminal amidation. AF647-labeled peptide has the sequence CKVDISSQISSMNQSLQQSKDYIKEAQRLLDTV and was labeled at the N-terminal cysteine with AF647 maleimide.

### Preparation of SLB substrates for NiV ectodomain experiments

All lipids were purchased from Avanti Polar Lipids with the exception of ATTO390-DOPE (ATTO-TEC). Ni-NTA DOGS = 1,2-dioleoyl-sn-glycero-3-[(*N*-(5-amino-1-carboxypentyl)iminodiacetic acid)succinyl] (nickel salt). DOPC = 1,2-dioleoyl-sn-glycero-3-phosphocholine. DPPC = 1,2-dipalmitoyl-sn-glycero-3-phosphocholine.

SLBs in sticky-Slide VI 0.4 (ibidi GmbH) chambers were made according to previously published protocols (*65*). Briefly, 1.5H cover glasses were cleaned in Piranha solution and adhered to the sticky-Slide. Two percent Ni-NTA DOGS in (DOPC) liposomes were

made by sonication in tris-buffered saline (TBS) [20 mM tris (pH 7.4) and 136 mM NaCl] and ruptured in the sticky-Slide chambers. The resulting bilayers were blocked with bovine serum albumin (BSA), followed by washing with TBS. All lipids used were purchased from Avanti Polar Lipids.

One hundred microliters of 10 pM AF647-labeled NiV $G_{ecto}$-Wt-40 Å-pAzF in 25 nM unlabeled NiV $G_{ecto}$-Wt-40 Å was added to each chamber and incubated for 15 min. Unbound protein was washed out and the buffer was exchanged to Imaging buffer [0.2 mM β-mercaptoethanol, glucose oxidase (320 μg/ml), catalase (50 μg/ml), 0.2 mM glucose, 2 mM Trolox, and BSA (0.1 mg/ml) in Hepes-buffered saline (HBS)]. The composition of HBS is 20 mM Hepes (pH 7.4) and 136 mM NaCl. Sequential additions of 0.5 μl of ephrinB2-mNG protein at 200× the final concentration were added to the chamber, mixed, and imaged.

One hundred microliters of 10 pM AF647-labeled NiV $G_{ecto}$-Wt-40 Å-pAzF was mixed with varying final concentrations of unlabeled NiV $F_{ecto}$ in HBS, added to each chamber, and incubated for 15 min. Unbound protein was washed out and the buffer was exchanged to Imaging buffer before imaging. Videos were recorded at 20-ms exposure per frame.

### Preparation of patterned SLB substrates for live-cell overlay experiments

Liposome suspensions were made according to previously published protocols (*65*). Briefly, 4% Ni-NTA DOGS in DOPC liposomes were made by sonication in water and diluted ½ with TBS just before use. Twenty-five-millimeter-diameter 1.5H cover glasses were cleaned in Piranha solution and stored in distilled water. Cover glasses were plasma-cleaned for 3 min just before incubating facedown on 30 μl of 0.1 mg/ml PLL(20)-g[3.5]-PEG (2)/PEG(3.4)-biotin (50%) (SuSoS) for at least 2 hours. PLL-PEG–coated cover glasses were washed with distilled water and then adhered 1.5 μl of water to a quartz photomask with 4-μm circular holes. The PLL-PEG is then etched by ultraviolet (UV) light in a UVO-Cleaner for 9 min. SLBs are formed only in the UV-etched circles by incubating the cover glasses facedown on 30 μl of liposome suspension for 3 min. The cover glasses are assembled into Attofluor cell chambers while immersed in water and then exchanged into TBS. The surface was blocked with 0.05% BSA overnight at 4°C. The PLL-PEG-biotin is incubated with DyLight-405 NeutrAvidin (1 μg/ml; Thermo Fisher Scientific) for 5 min and then Cyclo[Arg-Gly-Asp-D-Phe-Lys(Biotin)] (1 μg/ml; Peptides International). Ni-NTA groups on the SLB were functionalized by adding fluorophore-labeled ephrinB2 or scFv5B3 to a final concentration of approximately 50 nM. Unless otherwise specified, the composition of lipids used in patterned lipid bilayers was 4% Ni-NTA-DOGS in DOPC. DPPC bilayers were composed of 4% Ni-NTA-DOGS in DPPC.

### Preparation of plain SLB substrates for live-cell overlay experiments

Twenty-five-millimeter-diameter 1.5H cover glasses were cleaned in Piranha solution and stored in distilled water. Cover glasses were plasma-cleaned for 3 min just before incubating facedown on 30 μl of liposome suspension for 3 min. The cover glasses are assembled into Attofluor cell chambers while immersed in water and then exchanged into TBS. The surface was blocked with 0.05% BSA for 1 hour at 37°C. The composition of lipids used in plain lipid bilayers was 1% Ni-NTA-DOGS in DOPC for HRB binding experiments and 1% Ni-NTA-DOGS and 4% TR-DHPE in DOPC for hemifusion detection experiments.

### Preparation of PEGylated-SLB substrates for live-cell overlay experiments

Twenty-five-millimeter-diameter 1.5H cover glasses were cleaned in Piranha solution and stored in distilled water. Cover glasses were plasma-cleaned for 3 min, washed in water, and then dried under a nitrogen stream just before silanization in 2% aminopropyltriethoxysilane in ethanol for 1 hour at room temperature. The cover glasses were washed in ethanol followed by water and sonicated for 5 min in water. The cover glasses were then cured at 80°C for 30 min. One- to two-milligram aliquots of NTA-PEG3400-NHS (Nanocs) were dissolved in 0.1 M sodium bicarbonate and 0.8 M sodium sulfate until the cloud point is reached (typically 100 to 200 μl). The solution was then diluted with 0.1 M sodium bicarbonate to 80% of the PEG concentration at cloud point. After cooling to room temperature, the silanized cover glasses were placed facedown on 30 μl of the PEG solution and incubated at room temperature in a sealed petri dish for 2 hours. Unbound PEG was washed away with water. For immobilized ephrinB2 samples, the substrates were dried under a nitrogen stream before incubating facedown on 30 μl of 25 mM tris (pH 7.5), 150 mM sodium chloride, and 50 mM nickel chloride for 15 min. Otherwise, this step is omitted. The substrates were assembled into Attofluor chambers. Liposome solutions were diluted 1/8 in 0.5× TBS and 400 μl was added to the chamber. The lipid composition for immobilized ephrinB2 substrates was 0.04% ATTO 390-DOPE and 0.06% biotin-DHPE in DOPC, and the lipid composition for unrestrained ephrinB2 substrates was 0.04% ATTO 390-DOPE, 0.06% biotin-DHPE, and 2% Ni-NTA-DOGS in DOPC.

### Live-cell overlay on SLB substrates for TIRF microscopy

Chinese hamster ovary cells in six-well plates were transfected with 1 μg of NiV G construct in pCAGGS, 1 μg of NiV F construct in pCAGGS, 2 μl of Plus Reagent, and 5 μl of Lipofectamine LTX and incubated overnight. For imaging of fluorescence protein-tagged NiV proteins, cells were harvested with phosphate-buffered saline (PBS) formulated without calcium and magnesium. Transfected cells were labeled with PA-JF646-Halo (gift from L. Lavis). PA-JF646-Halo (20 nM) was incubated with cells for 30 min to allow optimal labeling. Unbound dyes were washed out with medium. Cells were then detached from culture dishes by nonenzymatic cell dissociation solution (Corning CellStripper).

Harvested cells were resuspended in cell imaging buffer (25 mM tris, 140 mM sodium chloride, 3 mM potassium chloride, 2 mM calcium chloride, 1 mM magnesium chloride, and 5.5 mM D-glucose). Buffer in the Attofluor chambers was exchanged to cell imaging buffer, and the chambers were equilibrated to 37°C. If cells are to be imaged in the presence of HRB peptide, then HRB peptide was added to a final concentration of approximately 0.5 μM before cell addition. If cells are to be imaged in the presence of drugs, Latrunculin A was added to a final concentration of approximately 1 μM and blebbistatin to 10 μM before cell addition. Cells were added to the chamber and allowed to interact with the substrates for 30 min before imaging.

Cell-substrate interfaces were imaged by TIRF microscopy on a Nikon Eclipse Ti-E inverted microscope with a 1.49 numerical aperture (NA) 100× objective. Samples were illuminated with a custom-built

launch that includes 405-, 488-, 561-, and 640-nm diode lasers. Fluorescence signal was generated in the blue (ex = 405 nm, em = 470/24 nm), green (ex = 488 nm, em = 525/50 nm), red (ex = 561 nm, em = 600/50 nm), and far-red channels (ex = 640 nm, em = 700/75 nm). Images were recorded with an Andor iXon897 EMCCD (electron-multiplying charge-coupled device) camera. The system is automated by the open source microscopy software Micro-Manager (*66*).

Time-lapse single-molecule imaging of PA-JF646 was performed by TIRF microscopy. Signal-to-noise and temporal resolution were optimized by minimizing laser power and maximizing video rate. To increase tracking accuracy, the density of individual PA-JF646 molecules was controlled by 405-nm laser illumination to be about ~0.05/$\mu m^2$. In cells spreading on Alexa 488–labeled ephrinB2 or scFv5B3 substrates, blue channel [ex = 405 nm, em = 470 (24) nm] and green channel [ex = 488 nm, em = 525 (50) nm] images were acquired before single-molecule recording to localize NeuTravidin and ephrinB2 patterns. After photoactivation, a small amount of JF-646 molecules were visualized and recorded in the far-red channel by an EMCCD camera with 20 fps (frames per second) video rate. Each movie contains 1000 frames for further analysis.

### Confocal microscopy for hemifusion detection

Cells overlaid on substrates were imaged at selected planes (5 nm and 5 μm above the cover glass) on a Nikon Eclipse Ti-E inverted microscope with a Yokogawa CSU-X1 spinning disk confocal unit and a 1.49 NA 100× objective. Samples were illuminated with a custom-built launch that includes 405-, 488-, 561-, and 640-nm diode lasers. Fluorescence signal was generated in the green (ex = 488 nm, em = 525/50 nm) and red (ex = 561 nm, em = 525/50 nm) channels. Images were recorded with an Andor iXon897 EMCCD camera. The system is automated by the open source microscopy software Micro-Manager (*66*).

### Single-particle tracking

Tracks were identified from single-particle movies with Trackmate (*67*). Every fourth image was used for track displacement measurement for NiV G ectodomain tracking videos. Every image was used for track displacement measurement for pa-JF646-NiV F-Halo tracking videos. Probability density distributions were calculated from the displacements of NiV G ectodomain tracks with Matlab (MathWorks). More than 5000 tracks and >200,000 displacements were typically used for each sample. Displacements of NiV F-Halo were sorted by their location using the Matlab script in data S1. Probability distributions of NiV F-Halo displacements inside and outside bilayer areas were calculated with OriginPro (OriginLab). More than 3000 tracks and >150,000 displacements were typically used for each sample. Tracks of NiV F-Halo were sorted by their location using the Matlab script in data S2. Immobile particle fractions were determined using the Matlab script in data S3.

### Quantification of HRB fluorescence

The following procedure was used for comparison of HRB binding to cells in the presence or absence of ephrinB2 and with wild-type or disulfide-bond mutant NiV F. Cell areas are identified by thresholding in Fiji (*68*) in the red channel where mCherry fluorescence is detected above background. SLB areas are identified by ephrinB2-AF488 fluorescence in the green channel. Regions of interest were created from the cell and bilayer areas, and cell areas not in the bilayers (cell background area) were used to calculate an average background value in the far-red channel. This value was subtracted from each pixel of the image in the far-red channel and then histograms of HRB fluorescence intensities were obtained from bilayer areas. Probability distributions from three cells were averaged.

### Analytical size exclusion chromatography

EphrinB2 protein was mixed with 10 μg of NiV G ectodomain in 100 μl of 50 mM tris (pH 7.5) and 150 mM NaCl at the indicated molar ratio. Samples were injected at 100-μl injection volumes and run at 0.2 ml/min on a S200 5/150 GL column with 3-ml bed volume. Sizing standards were blue dextran (2000 kDa, void volume), thyroglobulin (664 kDa), apoferritin (443 kDa), β-amylase (200 kDa), and BSA (66 kDa) (Sigma-Aldrich).

### Flow cytometry assay for cell surface expression of NiV proteins

Cells in 24-well tissue culture plates were transfected with 0.75 μg of NiV G construct in pCAGGS, 0.75 μg of NiV F construct in pCAGGS, 1.5 μl of Plus Reagent, and 1.5 μl of Lipofectamine (Life Technologies). After overnight incubation, cells were harvested with enzyme-free cell dissociation buffer, PBS (Life Technologies), and resuspended in fluorescence-activated cell sorting (FACS) buffer (1× PBS, Corning Cellgro; 1% BSA). A total of 50,000 cells per sample were incubated in 96-well conical bottom plates with either 0.2 μg of scFv1023 or 0.5 μg of mAb5B3 (gift from C. Broder) on ice for 30 min. scFv1023-stained cells were incubated with a 0.1-μg mouse anti-His monoclonal antibody conjugated to AF647 (BioLegend no. 906115) in 100 μl of FACS buffer on ice for 30 min. mAb5B3-stained cells were incubated with 0.1 μg of goat anti-mouse immunoglobulin G (IgG) polyclonal antibody conjugated to AF647 (BioLegend no. 405322) in 100 μl of FACS buffer on ice for 30 min. Samples were washed after each antibody incubation by centrifugation and resuspension in 150 μl of FACS buffer twice. Samples were then fixed with 1% paraformaldehyde on ice for 5 min and then filtered by centrifugation through a 0.4-μm MultiScreen Permeability Filter Plate (Millipore #MPC4NTR10). Data were collected with a BD Accuri C6 flow cytometer.

### Luciferase assay for fusion activity of NiV proteins

Cells in 24-well tissue culture plates were transfected with 0.5 μg of NiV G construct in pCAGGS, 0.5 μg of NiV F construct in pCAGGS, 0.0625 μg of T7-luciferase plasmid, 1.2 μl of Plus Reagent, and 1 μl of Lipofectamine (Life Technologies). After overnight incubation, cells were overlaid with BSR-T7 cells and incubated for 4 hours. Cells were then lysed in Glo-Lysis buffer (Promega), and luciferase activity was measured using Bright-Glo Reagent (Promega) with a Synergy 4 plate reader (Biotek).

### DNA sequences

***NiVG_SalI-ClaI_40Ålink***

AAAGCAGGCTTTAAAGGAACCAATTCAGTCGACACCATGCTGTCCGCCATCGTGCTGTACGTGCTGCTGGCCGCCGCCGCCCACAGCGCCTTCGCCCACCACCACCACCACCACCCCCCTGACGACGATGATAAACTGGGAGTGTCCAGCAGCGAGGTGTCCAACGTGGAAGCCGATTCTGCCGCCCAGAATTACACCCGGAGCACCGACAATCAGGCCGTGATCAAAGATGCCCTGCAGGGCATTCAGCAGCAGATTAAGGGACTGGCCGACAAAATCGGGACCGAAATTGGACCCAAGGTGAGCCTGATCGATACCAGCAGCACAATTACAATTCCC.

***scFv1023***

CAGGCTTTAAAGGAACCAATTCAGTCGACAAGCTTAC-CATGGAACTGGGCCTGAGATGGGTGTTCCTGGTGGC-CATCCTGGAAGGCGTGCAGTGCGAGGTGCAACTGGTC-CAGTCTGGCGCCGACGTGAAGAAACCCGGCAGCAGCGT-GAAGGTGTCCTGCAAGTCTAGCGGCGGCACCTTCTCTA-AGTACGCCATCAACTGGGTGCGCCAGGCCCCTGGACAG-GGCCTGGAATGGATGGGCGGCATCATCCCCATCCTGG-GAATCGCCAACTACGCCCAGAAATTCCAGGGCAGAGT-GACCATCACCACCGACGAGAGCACCAGCACCGCCTATAT-GGAACTGAGCAGCCTGCGGAGCGAGGACACCGCCGTG-TACTATTGTGCCAGAGGCTGGGGCAGAGAGCAGCTGGC-CCCTCACCCTAGCCAGTACTACTACTATTACTACGGCAT-GGACGTGTGGGGCCAGGGCACCACCGTGACAGTGT-CATCTGGTACCGGCGGATCTGGCGGCGGAGGAAGCG-GAGGCGGAGGATCAGGCGGAGCTAGCGAGATCGTGAT-GACCCAGAGCCCTGGCACCCTGTCTCTGGCCCCTGGC-GAAAGAGCCACCCTGAGCTGTTGGGCCTCTCAGAGCGTG-CGGAACAACTACCTGGCCTGGCACCAGCAGAAGCCCGG-ACAGGCTCCTCGGCTCGTGATCTACAACGGCAGCACCA-GAGCCACCGGCATCCCCGATAGATTTTCCGGCTCTGG-CAGCGGCACCGACTTCACCCTGACCATCAGCAGACTG-GACCCCGAGGACTTCGCTGTGTACTACTGCCAGCAGTAC-GGCAACTCCAGAAGAGTGACCTTCGGCGGAGGCAC-CAAGGTGGAAATCAAGCGGATCGAGGGCCGGCACCAC-CATCACCATCATCACCACTGAGCGGCCGCACTCGAGA-TATCTAGACCCAGCTT.

***scFv5B3***

GCAAAAGAATTCACCATGGAAACGGACACCCTGCTGCT-GTGGGTGCTGTTGTTGTGGGTGCCAGGATCTACAGGCGC-CGAGGTGCAGCTTGTTGAATCTGGCGGAGGCCTGGTTA-AGCCTGGCGGATCTCTGAAGCTGAGCTGTGCCGCCAGCG-GCTTCACCTTCAGCAGCTACGATATGAGCTGGGTCCGA-CAGACCCCTGAGAAGAGACTGGAATGGGTCGCCATGAT-CAGCAGCGGCGGCAGCTACAGCTACTACCCCGATTCTGT-GAAGGGCAGATTCACCATCAGCCGGGACAACGC-CAAGAACACCCTGTACCTGCAGATGAGCAGCCCT-GAGAAGCGAGGACACCGCCATGTACTACTGTGCCAGA-CAGGGCGACTACGCTTGGTTTGCCTATTGGGGCCAGGG-CACCCTGGTTACAGTTTCTGGTGGCGGAGGAAGCGGAG-GCGGAGGATCAGGTGGCGGTGGATCTGACATCCAGATG-ACACAGAGCCCTGCCAGCCAGTCTGCCTCTCTGGGA-GAGTCTGTGACCATCACATGTCTGGCCAGCCAGACCATC-GGAACATGGCTGGCTTGGTATCAGCAGAAGCCCGG-CAAGTCTCCCCAGCTCCTGATCTATGCCGCCACATCTCT-GGCTGATGGCGTGCCCTCTAGATTTTCTGGCTCTGGCAG-CGGCACCAAGTTCAGCTTTAAGATCAGCTCCCTGCAGGC-CGAGGACTTCGTGTCCTACTACTGCCAGCAGTTCTACAG-CACCCCTTTCACCTTTGGCGGCGGAACAAAGCTGGAAAT-CAAGCGGAAAGAAACCGCCGCTGCCAAGTTCGAGCGG-CAGCACATGGATTCTATCGAGGGCAGAAGCGGCCAC-CACCATCATCACCATCACCACTGAGCTAGCAGATC.

***Primer sequences***

NiVGect_40AlinkAmber_For: CGATTCTGCCGCCCAGAATTA-CACCCG.

NiVGect_40AlinkAmber_Rev: GCTTCCACGTTGGACTACTC-GCTGCTGGACAC.

NiVGect_V182A_Q5_For: GTGTCCAACCTGGCCGGACTG-CCCAACAAC.

NiVGect_V182A_Q5_Rev: TCCCTCGGTCTGTGGGCGGTACTC.

mNeonGreen_For: GCAGTCGACGGTACCGGTCGCCAC-CATGGTGTCCAAGGGCGAAGAGG.

mNeonGreen_Rev: CCTTGCCGGCCTCGAGCGGCCGCTAGCT-CACTTGTACAGCTCGTCCATGCC.

pTT5_EcoRI_For: CCCAGGTCCAAGTTTAAACGGATCTCTAG-CGAATTC.

pTT5_NotI_Rev: CCCTTGCCGGCCTCGAGCGGCC.

IgG1-Fc_splitlink_Rev: ACCGGTACCGTCGACTGCAGAATCTTC-CCGGGGGACAGGGAC.

EphB2-167_splitlink_Rev: ACCGGTACCGTCGACTG-CAGAATGTCCTGGCCCACTTTCATCAGGATC.

EphB2-229-XA-His8_Rev: GCCGCTAGCTTAGTGATGGT-GATGGTGGTGATGGTGAGGGTCCATCCGGCCCTCG.

pCG_SacI_mNG_For: CATCATTTTGGCAAAGAATTC-GAGCTCATGGTGTCCAAGGGCGAAGAGG.

mNG_GSlink_NiVGfull_Rev: CTAACTTTCTTGTTTTCTGC-CGGCATTCCACCTCCGCCAGATCCTCCGCCAC-CAGACTTGTACAGCTCGTCCATGCCCATC.

NiVGfull_Nterm_For: ATGCCGGCAGAAAACAAGAAAGTTAG.

NiVGfull_KpnI640_Rev: CAGCAATGGGTCTGTGATACAG-GTACC.

NiVFfull_EcoRV_For: GTCTTTACAGATAAAGTTGA-TATATCAAGTCAGATATC.

NiVFfull_Cterm_Rev: TGTCCCAATGTAGTAGAGATCCCCAC.

NiVFfull_link_CyOFP_For: GTGGGGATCTCTACTA-CATTGGGACAGGAGGCGGAGGATCTGGTGGCG-GAGATCCTATGGTGAGCAAGGGCGAG.

mScarlet-I_pCG_Gib_Rev: CATAATTTTTGGCAGAGG-GAAAAAGATCTGCTAGCTTACTTGTACAGCTCGTCCATG-CCG.

NiVfull_119C Rev.: CAAACTCCTGCCATTATAACTCCG-GCTAATC.

NiVFfull_110C_119C_For: TAGCCGGAGTTATAATGG-CAGGAGTTTGCATTGGGATTGCAACC.

NiVFfull_100C-119C_Rev: ATCTCACATCACCGACAAGGT-CATGAGTGCAGTTTTTGTAGATCTCTAACGC.

NiVFfull_100C_For: GAGATCTACAAAAACTGCACTCAT-GACCTTGTCGG.

NiVFfull-link-Halo_For: GGGATCTCTACTACATTGGGA-CAGGAGGCGGAGGATCTGGTGGCGGAGATCCTATGG-CAGAAATCGGTACTGGCTTTC.

Halo_pCG_Rev: GGCAGAGGGAAAAAGATCTGCTAGCT-TAGCCGGAAATCTCGAGCGTCGACAGC.

pCG-SacI-Halo_For: CTCATCATTTTGGCAAAGAATTC-GAGCTCATGGCAGAAATCGGTACTGGCTTTC.

Halotag-GSlink-NiVGfull_Rev: CTAACTTTCTTGTTTTCTG-CCGGCATTCCACCTCCGCCAGATCCTCCGCCACCAGAGC-CGGAAATCTCGAGCGTCGACAG.

## SUPPLEMENTARY MATERIALS

Supplementary material for this article is available at http://advances.sciencemag.org/cgi/content/full/7/5/eabe1235/DC1

View/request a protocol for this paper from *Bio-protocol*.

## REFERENCES AND NOTES

1. M. Kielian, Mechanisms of virus membrane fusion proteins. *Annu. Rev. Virol.* **1**, 171–189 (2014).
2. F. A. Rey, S.-M. Lok, Common features of enveloped viruses and implications for immunogen design for next-generation vaccines. *Cell* **172**, 1319–1334 (2018).

3. S. Bose, T. S. Jardetzky, R. A. Lamb, Timing is everything: Fine-tuned molecular machines orchestrate paramyxovirus entry. *Virology* **479-480**, 518–531 (2015).
4. K. Sathiyamoorthy, J. Chen, R. Longnecker, T. S. Jardetzky, The COMPLEXity in herpesvirus entry. *Curr. Opin. Virol.* **24**, 97–104 (2017).
5. H.-S. Yin, X. Wen, R. G. Paterson, R. A. Lamb, T. S. Jardetzky, Structure of the parainfluenza virus 5 F protein in its metastable, prefusion conformation. *Nature* **439**, 38–44 (2006).
6. P. Yuan, K. A. Swanson, G. P. Leser, R. G. Paterson, R. A. Lamb, T. S. Jardetzky, Structure of the Newcastle disease virus hemagglutinin-neuraminidase (HN) ectodomain reveals a four-helix bundle stalk. *Proc. Natl. Acad. Sci. U.S.A.* **108**, 14920–14925 (2011).
7. M. A. Brindley, R. K. Plemper, Blue native PAGE and biomolecular complementation reveal a tetrameric or higher-order oligomer organization of the physiological measles virus attachment protein H. *J. Virol.* **84**, 12174–12184 (2010).
8. T. S. Jardetzky, R. A. Lamb, Activation of paramyxovirus membrane fusion and virus entry. *Curr. Opin. Virol.* **5**, 24–33 (2014).
9. J.-L. Palgen, E. M. Jurgens, A. Moscona, M. Porotto, L. M. Palermo, Unity in diversity: Shared mechanism of entry among paramyxoviruses. *Prog. Mol. Biol. Transl. Sci.* **129**, 1–32 (2015).
10. Q. Liu, J. A. Stone, B. Bradel-Tretheway, J. Dabundo, J. A. Benavides Montano, J. Santos-Montanez, S. B. Biering, A. V. Nicola, R. M. Iorio, X. Lu, H. C. Aguilar, Unraveling a three-step spatiotemporal mechanism of triggering of receptor-induced Nipah virus fusion and cell entry. *PLOS Pathog.* **9**, e1003770 (2013).
11. N. Ader-Ebert, M. Khosravi, M. Herren, M. Avila, L. Alves, F. Bringolf, C. Örvell, J. P. Langedijk, A. Zurbriggen, R. K. Plemper, P. Plattet, Sequential conformational changes in the morbillivirus attachment protein initiate the membrane fusion process. *PLOS Pathog.* **11**, e1004880 (2015).
12. C. K. Navaratnarajah, N. Oezguen, L. Rupp, L. Kay, V. H. J. Leonard, W. Braun, R. Cattaneo, The heads of the measles virus attachment protein move to transmit the fusion-triggering signal. *Nat. Struct. Mol. Biol.* **18**, 128–134 (2011).
13. C. T. Pager, W. W. Craft Jr., J. Patch, R. E. Dutch, A mature and fusogenic form of the Nipah virus fusion protein requires proteolytic processing by cathepsin L. *Virology* **346**, 251–257 (2006).
14. K. N. Bossart, L.-F. Wang, M. N. Flora, K. B. Chua, S. K. Lam, B. T. Eaton, C. C. Broder, Membrane fusion tropism and heterotypic functional activities of the Nipah virus and Hendra virus envelope glycoproteins. *J. Virol.* **76**, 11186–11198 (2002).
15. J. K. Lee, A. Prussia, T. Paal, L. K. White, J. P. Snyder, R. K. Plemper, Functional interaction between paramyxovirus fusion and attachment proteins. *J. Biol. Chem.* **283**, 16561–16572 (2008).
16. S. Bose, A. S. Song, T. S. Jardetzky, R. A. Lamb, Fusion activation through attachment protein stalk domains indicates a conserved core mechanism of paramyxovirus entry into cells. *J. Virol.* **88**, 3925–3941 (2014).
17. S. Bose, C. M. Heath, P. A. Shah, M. Alayyoubi, T. S. Jardetzky, R. A. Lamb, Mutations in the parainfluenza virus 5 fusion protein reveal domains important for fusion triggering and metastability. *J. Virol.* **87**, 13520–13531 (2013).
18. M. A. Brindley, R. Suter, I. Schestak, G. Kiss, E. R. Wright, R. K. Plemper, A stabilized headless measles virus attachment protein stalk efficiently triggers membrane fusion. *J. Virol.* **87**, 11693–11703 (2013).
19. M. Avila, M. Khosravi, L. Alves, N. Ader-Ebert, F. Bringolf, A. Zurbriggen, R. K. Plemper, P. Plattet, Canine distemper virus envelope protein interactions modulated by hydrophobic residues in the fusion protein globular head. *J. Virol.* **89**, 1445–1451 (2015).
20. N. Ader, M. Brindley, M. Avila, C. Örvell, B. Horvat, G. Hiltensperger, J. Schneider-Schaulies, M. Vandevelde, A. Zurbriggen, R. K. Plemper, P. Plattet, Mechanism for active membrane fusion triggering by morbillivirus attachment protein. *J. Virol.* **87**, 314–326 (2012).
21. J. A. Stone, B. M. Vemulapati, B. Bradel-Tretheway, H. C. Aguilar, Multiple strategies reveal a bidentate interaction between the Nipah virus attachment and fusion glycoproteins. *J. Virol.* **90**, 10762–10773 (2016).
22. V. R. Melanson, R. M. Iorio, Amino acid substitutions in the F-specific domain in the stalk of the newcastle disease virus HN protein modulate fusion and interfere with its interaction with the F protein. *J. Virol.* **78**, 13053–13061 (2004).
23. R. K. Plemper, A. L. Hammond, D. Gerlier, A. K. Fielding, R. Cattaneo, Strength of envelope protein interaction modulates cytopathicity of measles virus. *J. Virol.* **76**, 5051–5061 (2002).
24. K. A. Bishop, T. S. Stantchev, A. C. Hickey, D. Khetawat, K. N. Bossart, V. Krasnoperov, P. Gill, Y. R. Feng, L. Wang, B. T. Eaton, L.-F. Wang, C. C. Broder, Identification of Hendra virus G glycoprotein residues that are critical for receptor binding. *J. Virol.* **81**, 5893–5901 (2007).
25. R. Mattera, G. G. Farias, G. A. Mardones, J. S. Bonifacino, Co-assembly of viral envelope glycoproteins regulates their polarized sorting in neurons. *PLOS Pathog.* **10**, e1004107 (2014).
26. M. Porotto, S. G. Palmer, L. M. Palermo, A. Moscona, Mechanism of fusion triggering by human parainfluenza virus type III: Communication between viral glycoproteins during entry. *J. Biol. Chem.* **287**, 778–793 (2011).
27. Q. Yao, X. Hu, R. W. Compans, Association of the parainfluenza virus fusion and hemagglutinin-neuraminidase glycoproteins on cell surfaces. *J. Virol.* **71**, 650–656 (1997).
28. H. C. Aguilar, K. A. Matreyek, C. M. Filone, S. T. Hashimi, E. L. Levroney, O. A. Negrete, A. Bertolotti-Ciarlet, D. Y. Choi, I. McHardy, J. A. Fulcher, S. V. Su, M. C. Wolf, L. Kohatsu, L. G. Baum, B. Lee, N-glycans on Nipah virus fusion protein protect against neutralization but reduce membrane fusion and viral entry. *J. Virol.* **80**, 4878–4889 (2006).
29. M. Porotto, I. DeVito, S. G. Palmer, E. M. Jurgens, J. L. Yee, C. C. Yokoyama, A. Pessi, A. Moscona, Spring-loaded model revisited: Paramyxovirus fusion requires engagement of a receptor binding protein beyond initial triggering of the fusion protein. *J. Virol.* **85**, 12867–12880 (2011).
30. P. Plattet, L. Alves, M. Herren, H. C. Aguilar, Measles virus fusion protein: Structure, function and inhibition. *Viruses* **8**, 112 (2016).
31. G. Arunkumar, R. Chandni, D. T. Mourya, S. K. Singh, R. Sadanandan, P. Sudan, B. Bhargava; Nipah Investigators People and Health Study Group, Outbreak investigation of Nipah virus disease in Kerala, India, 2018. *J. Infect. Dis.* **219**, 1867–1878 (2019).
32. A. S. Ambat, S. M. Zubair, N. Prasad, P. Pundir, E. Rajwar, D. S. Patil, P. Mangad, Nipah virus: A review on epidemiological characteristics and outbreaks to inform public health decision making. *J. Infect. Public Health* **12**, 634–639 (2019).
33. N. Thakur, D. Bailey, Advances in diagnostics, vaccines and therapeutics for Nipah virus. *Microbes Infect.* **21**, 278–286 (2019).
34. K. Xu, Y.-P. Chan, B. Bradel-Tretheway, Z. Akyol-Ataman, Y. Zhu, S. Dutta, L. Yan, Y. Feng, L.-F. Wang, G. Skiniotis, B. Lee, Z. H. Zhou, C. C. Broder, H. C. Aguilar, D. B. Nikolov, Crystal structure of the pre-fusion Nipah virus fusion glycoprotein reveals a novel hexamer-of-trimers assembly. *PLOS Pathog.* **11**, e1005322 (2015).
35. O. A. Negrete, M. C. Wolf, H. C. Aguilar, S. Enterlein, W. Wang, E. Mühlberger, S. V. Su, A. Bertolotti-Ciarlet, R. Flick, B. Lee, Two key residues in ephrinB3 are critical for its use as an alternative receptor for Nipah virus. *PLOS Pathog.* **2**, e7 (2006).
36. H. C. Aguilar, V. Aspericueta, L. R. Robinson, K. E. Aanensen, B. Lee, A quantitative and kinetic fusion protein-triggering assay can discern distinct steps in the nipah virus membrane fusion cascade. *J. Virol.* **84**, 8033–8041 (2010).
37. Q. Liu, L. Chen, H. C. Aguilar, K. C. Chou, A stochastic assembly model for Nipah virus revealed by super-resolution microscopy. *Nat. Commun.* **9**, 3050 (2018).
38. J. K. Chung, Y. K. Lee, J.-P. Denson, W. K. Gillette, S. Alvarez, A. G. Stephen, J. T. Groves, K-Ras4B remains monomeric on membranes over a wide range of surface densities and lipid compositions. *Biophys. J.* **114**, 137–145 (2018).
39. Z. Chen, D. Oh, K. H. Biswas, C.-H. Yu, R. Zaidel-Bar, J. T. Groves, Spatially modulated ephrinA1:EphA2 signaling increases local contractility and global focal adhesion dynamics to promote cell motility. *Proc. Natl. Acad. Sci. U.S.A.* **115**, E5696–E5705 (2018).
40. G. Valbuena, H. Halliday, V. Borisevich, Y. Goez, B. Rockx, A human lung xenograft mouse model of Nipah virus infection. *PLOS Pathog.* **10**, e1004063 (2014).
41. J. J. W. Wong, T. A. Young, J. Zhang, S. Liu, G. P. Leser, E. A. Komives, R. A. Lamb, Z. H. Zhou, J. Salafsky, T. S. Jardetzky, Monomeric ephrinB2 binding induces allosteric changes in Nipah virus G that precede its full activation. *Nat. Commun.* **8**, 781 (2017).
42. P. G. Saffman, M. Delbrück, Brownian motion in biological membranes. *Proc. Natl. Acad. Sci. U.S.A.* **72**, 3111–3113 (1975).
43. Y. Kaizuka, J. T. Groves, Structure and dynamics of supported intermembrane junctions. *Biophys. J.* **86**, 905–912 (2004).
44. J. D. Knight, M. G. Lerner, J. G. Marcano-Velázquez, R. W. Pastor, J. J. Falke, Single molecule diffusion of membrane-bound proteins: Window into lipid contacts and bilayer dynamics. *Biophys. J.* **99**, 2879–2887 (2010).
45. W.-C. Lin, L. Iversen, H.-L. Tu, C. Rhodes, S. M. Christensen, J. S. Iwig, S. D. Hansen, W. Y. C. Huang, J. T. Groves, H-Ras forms dimers on membrane surfaces via a protein-protein interface. *Proc. Natl. Acad. Sci. U.S.A.* **111**, 2996–3001 (2014).
46. K. H. Biswas, J. T. Groves, Hybrid live cell-supported membrane interfaces for signaling studies. *Annu. Rev. Biophys.* **48**, 537–562 (2019).
47. H. C. Aguilar, R. M. Iorio, Henipavirus membrane fusion and viral entry. *Curr. Top. Microbiol. Immunol.* **359**, 79–94 (2012).
48. K. N. Bossart, D. L. Fusco, C. C. Broder, Paramyxovirus entry. *Adv. Exp. Med. Biol.* **790**, 95–127 (2013).
49. J. J. W. Wong, R. G. Paterson, R. A. Lamb, T. S. Jardetzky, Structure and stabilization of the Hendra virus F glycoprotein in its prefusion form. *Proc. Natl. Acad. Sci. U.S.A.* **113**, 1056–1061 (2015).
50. Y.-P. Chan, M. Lu, S. Dutta, L. Yan, J. Barr, M. Flora, Y.-R. Feng, K. Xu, D. B. Nikolov, L.-F. Wang, G. Skiniotis, C. C. Broder, Biochemical, conformational, and immunogenic analysis of soluble trimeric forms of henipavirus fusion glycoproteins. *J. Virol.* **86**, 11457–11471 (2012).
51. H. V. Dang, Y.-P. Chan, Y.-J. Park, J. Snijder, S. C. Da Silva, B. Vu, L. Yan, Y.-R. Feng, B. Rockx, T. W. Geisbert, C. E. Mire, C. C. Broder, D. Veesler, An antibody against the F glycoprotein inhibits Nipah and Hendra virus infections. *Nat. Struct. Mol. Biol.* **26**, 980–987 (2019).
52. J. J. Otterstrom, B. Brandenburg, M. H. Koldijk, J. Juraszek, C. Tang, S. Mashaghi, T. Kwaks, J. Goudsmit, R. Vogels, R. H. E. Friesen, A. M. van Oijen, Relating influenza virus membrane

fusion kinetics to stoichiometry of neutralizing antibodies at the single-particle level. *Proc. Natl. Acad. Sci. U.S.A.* **111**, E5143–E5148 (2014).
53. K. A. Baker, R. E. Dutch, R. A. Lamb, T. S. Jardetzky, Structural basis for paramyxovirus-mediated membrane fusion. *Mol. Cell* **3**, 309–319 (1999).
54. Z. Lou, Y. Xu, K. Xiang, N. Su, L. Qin, X. Li, G. F. Gao, M. Bartlam, Z. Rao, Crystal structures of Nipah and Hendra virus fusion core proteins. *FEBS J.* **273**, 4538–4547 (2006).
55. C. J. Russell, T. S. Jardetzky, R. A. Lamb, Membrane fusion machines of paramyxoviruses: Capture of intermediates of fusion. *EMBO J.* **20**, 4024–4034 (2001).
56. D. L. Floyd, J. R. Ragains, J. J. Skehel, S. C. Harrison, A. M. van Oijen, Single-particle kinetics of influenza virus membrane fusion. *Proc. Natl. Acad. Sci. U.S.A.* **105**, 15382–15387 (2008).
57. K. H. Biswas, K. L. Hartman, C.-h. Yu, O. J. Harrison, H. Song, A. W. Smith, W. Y. C. Huang, W.-C. Lin, Z. Guo, A. Padmanabhan, S. M. Troyanovsky, M. L. Dustin, L. Shapiro, B. Honig, R. Zaidel-Bar, J. T. Groves, E-cadherin junction formation involves an active kinetic nucleation process. *Proc. Natl. Acad. Sci. U.S.A.* **112**, 10932–10937 (2015).
58. R. E. Dutch, S. B. Joshi, R. A. Lamb, Membrane fusion promoted by increasing surface densities of the paramyxovirus F and HN proteins: Comparison of fusion reactions mediated by simian virus 5 F, human parainfluenza virus type 3 F, and influenza virus HA. *J. Virol.* **72**, 7745–7753 (1998).
59. L. V. Chernomordik, V. A. Frolov, E. Leikina, P. Bronk, J. Zimmerberg, The pathway of membrane fusion catalyzed by influenza hemagglutinin: Restriction of lipids, hemifusion, and lipidic fusion pore formation. *J. Cell Biol.* **140**, 1369–1382 (1998).
60. T. Ivanovic, J. L. Choi, S. P. Whelan, A. M. van Oijen, S. C. Harrison, Influenza-virus membrane fusion by cooperative fold-back of stochastically induced hemagglutinin intermediates. *eLife* **2**, e00333 (2013).
61. M. A. Wurth, R. M. Schowalter, E. C. Smith, C. L. Moncman, R. E. Dutch, R. O. McCann, The actin cytoskeleton inhibits pore expansion during PIV5 fusion protein-promoted cell-cell fusion. *Virology* **404**, 117–126 (2010).
62. C. Liu, J. X. Chin, D.-Y. Lee, SynLinker: An integrated system for designing linkers and synthetic fusion proteins. *Bioinformatics* **31**, 3700–3702 (2015).
63. G. Backliwal, M. Hildinger, V. Hasija, F. M. Wurm, High-density transfection with HEK-293 cells allows doubling of transient titers and removes need for a priori DNA complex formation with PEI. *Biotechnol. Bioeng.* **99**, 721–727 (2008).
64. T. Huber, S. Naganathan, H. Tian, S. Ye, T. P. Sakmar, Unnatural amino acid mutagenesis of GPCRs using amber codon suppression and bioorthogonal labeling. *Methods Enzymol.* **520**, 281–305 (2013).
65. W.-C. Lin, C.-H. Yu, S. Triffo, J. T. Groves, Supported membrane formation, characterization, functionalization, and patterning for application in biological science and technology. *Curr. Protoc. Chem. Biol.* **2**, 235–269 (2010).
66. A. D. Edelstein, M. A. Tsuchida, N. Amodaj, H. Pinkard, R. D. Vale, N. Stuurman, Advanced methods of microscope control using μManager software. *J. Biol. Methods* **1**, e10 (2014).
67. J.-Y. Tinevez, N. Perry, J. Schindelin, G. M. Hoopes, G. D. Reynolds, E. Laplantine, S. Y. Bednarek, S. L. Shorte, K. W. Eliceiri, TrackMate: An open and extensible platform for single-particle tracking. *Methods* **115**, 80–90 (2017).
68. J. Schindelin, I. Arganda-Carreras, E. Frise, V. Kaynig, M. Longair, T. Pietzsch, S. Preibisch, C. Rueden, S. Saalfeld, B. Schmid, J.-Y. Tinevez, D. J. White, V. Hartenstein, K. Eliceiri, P. Tomancak, A. Cardona, Fiji: An open-source platform for biological-image analysis. *Nat. Methods* **9**, 676–682 (2012).

**Acknowledgments:** We thank S. Saurabh for providing the pENTR4-Halotag plasmid. We thank L. Lavis for the gift of PA-JF646-Halo ligand. **Funding:** This work was supported by NIAID grant R01 AI137523 to T.S.J. and by National Institutes of Health (NIH) National Cancer Institute (NCI) Physical Sciences in Oncology Network (PS-ON) project 1-U01CA202241 and by the Novo Nordisk Foundation Challenge Program under the Center for Geometrically Engineered Cellular Systems to J.T.G. Z.C. is also funded by Shanghai Municipal Science and Technology Major Project ZJLab (2018SHZDZX01). **Author contributions:** J.J.W., Z.C., and J.K.C. performed experiments. J.J.W., Z.C., J.K.C., J.T.G., and T.S.J. analyzed data. J.J.W., Z.C., T.S.J., and J.T.G. wrote and edited the manuscript. **Competing interests:** The authors declare that they have no competing interests. **Data and materials availability:** All data needed to evaluate the conclusions in the paper are present in the paper and/or the Supplementary Materials. Additional data related to this paper may be requested from the authors.

Submitted 1 August 2020
Accepted 7 December 2020
Published 27 January 2021
10.1126/sciadv.abe1235

**Citation:** J. J. Wong, Z. Chen, J. K. Chung, J. T. Groves, T. S. Jardetzky, EphrinB2 clustering by Nipah virus G is required to activate and trap F intermediates at supported lipid bilayer–cell interfaces. *Sci. Adv.* **7**, eabe1235 (2021).